Master's thesis

NTNU
Norwegian University of Science and Technology
Faculty of Natural Sciences
Department of Physics

Thomas Gullvik Hines

Discrimination of Malignant and Non-Malignant Urinary Bladder Cells Using Microfluidic Constriction Deformation Cytometry

Master's thesis in Nanotechnology
Supervisor: Bjørn Torger Stokke
Co-supervisor: Ingrid Haga Øvreeide
July 2023

NTNU
Norwegian University of
Science and Technology

Thomas Gullvik Hines

Discrimination of Malignant and Non-Malignant Urinary Bladder Cells Using Microfluidic Constriction Deformation Cytometry

Master's thesis in Nanotechnology
Supervisor: Bjørn Torger Stokke
Co-supervisor: Ingrid Haga Øvreeide
July 2023

Norwegian University of Science and Technology
Faculty of Natural Sciences
Department of Physics

NTNU
Norwegian University of
Science and Technology

Abstract

Cancer is a leading cause of death worldwide, with one in six deaths being linked to cancer in 2020. To reduce the morbidity rate, screening and early diagnosis is crucial. Studies have shown that for some cancers, the stiffness or Young's modulus is reduced with increased metastatic potential. As a higher metastatic potential is associated with a higher morbidity rate, mechanical phenotyping of cells could be a propitious avenue for diagnosis.

The mechanical phenotype of a cell can be measured by single-cell techniques such as atomic force microscopy (AFM) or micropipette aspiration. These techniques provide low throughput measurements of cells and are demanding to use.

Deformation cytometry allows for high throughput analysis of single cells by utilizing microfluidics. A microfluidic constriction deformation cytometry platform has been developed during this thesis, where cells are guided through a microfluidic channel with a constriction region in which the channel dimensions are smaller than that of the cell. The pressure gradient forces cells to comply to a reduced channel dimension and to travel through a 300 µm long constriction region. The cells are observed through a microscope and recorded with a high-speed camera, and parameters such as entry time, transit time, exit time and area are gathered by a Python script.

In this work, the malignant bladder cancer cell line T24 and the non-malignant bladder epithelium cell line HCV29 are used. The results show some differences in transit time between malignant and non-malignant cell types. In particular, the malignant cells seem to have a less size-dependent transit time, meaning that the time it takes for the cells to be transported through the constriction channel is similar for smaller and larger cells, which could suggest a higher degree of deformability than the non-malignant cells.

Sammendrag

Kreft er en av de ledende dødsårsakene på verdensbasis og forårsaket en av seks dødsfall i 2020. For å redusere dødeligheten er screening og tidlig diagnose avgjørende. Studier gjort på forskjellige krefttyper, viser at for noen kreftformer reduseres stivheten eller Youngs modulus til kreftcellene parallelt med økende spredningspotensial. Et høyere spredningspotensial er assosiert med høyere dødelighet og mekanisk fenotyping av celler kan være en lovende teknikk for å stille diagnose.

Den mekaniske fenotypen til celler kan måles med enkelt-celle-teknikker som atomærkraftmikroskop (AFM) eller mikropipetteaspirasjon. Disse teknikkene gir en lav gjennomstrømming av celler, som vil si at det tar lang tid å analysere mange celler.

Deformasjonscytometri muliggjør høy gjennomstrømmingsanalyse for enkeltceller ved å utnytte mikrofluidikk. I denne hovedoppgaven har en mikrofluidisk plattform for å utføre deformasjonscytometri blitt utviklet, hvor celler ledes gjennom en konstriksjonsregion der tverrsnittet til kanalen er mindre enn cellens dimensjoner. Trykkgradienten tvinger celler til å deformeres for å få plass i kanalen og bevege seg gjennom en 300 µm lang konstriksjonsregion. Cellene observeres gjennom et lysmikroskop og filmes med et høyhastighetskamera, og parametere som inngangstid, passasjetid, utgangstid og areal innhentes av et Pythonscript.

I dette arbeidet har blærekreftceller fra den ondartede cellelinjen T24 blitt brukt, i tillegg til ikke-ondartede blære-epitelceller fra cellelinjen HCV29. Resultatene viser noen forskjeller mellom ondartede og ikke-ondartete celletyper. De ondartete cellene virker å ha en mindre størrelsesavhengig passasjetid, som vil si at tiden cellene bruker på å passere konstriksjonsregionen er relativt lik for store og små celler. Dette kan tyde på at disse cellene har en høyere grad av deformerbarhet enn ikke-ondartede.

Preface

This thesis marks the completion of my masters degree in Nanotechnology. The work was performed during the spring and summer of 2023, in addition to being related to the work I performed during the fall semester of 2022.

Firstly, I would like to thank Bjørn Torger Stokke for motivation, feedback and for guiding me through my final year of studies. I also want to extend my gratitude to Kartik Totlani for sharing his knowledge and experience with me. Jessica Monaldi and Ingrid Haga Øvreeide are also acknowledged for experimental assistance.

I want to express my genuine gratitude to Sylvie Lelu, Astrid Bjørkøy and Augusta Sundbø. Thank you for all the support and assistance throughout the year, it has been a pleasure working in your labs.

Thank you to the engineers in NanoLab for help throughout the year. In that regard, the Research Council of Norway is acknowledged for the support to the Norwegian Micro- and Nano-Fabrication Facility, NorFab, project number 295864.

Finally, I would like to thank my friends and family for their unwavering support, in particular my sister Hanne for words of encouragement and support, and my brother Joachim for his support and assistance with the implementation of the Python code.

Thomas Gullvik Hines

11th July 2023

Table of Contents

Abbreviations

ATP Adenosine Triphosphate

ADP Adenosine Diphosphate

GTP Guanosine Triphosphate

ECM Extracellular Matrix

CTC Circulating Tumor Cell

LOC Lab on a Chip

CDC Constriction Deformation Cytometry

SDC Shear Flow Deformation Cytometry

XDC Extensional Flow Deformation Cytometry

SMR Suspended Microchannel Resonator

PDMS Polydimethylsiloxane

IPA Isopropyl alcohol

UV Ultraviolet

RPM Revolutions per Minute

PBS Phosphate Buffered Saline

FBS Fetal Bovine Serum

EDTA Ethylenediaminetetraacetic acid

BSA Bovine Serum Albumin

NA Numerical Aperture

FPS Frames per Second

ROI Region of Interest

FEA Finite Element Analysis

TD Taylor Deformation

List of Tables

List of Figures

Chapter 1

Introduction

Cancer the is second leading cause of death globally, and one in six deaths are caused by cancer [1]. In Norway, 4 out of 10 people over the age of 80 have one or more cancer diagnosis, but 3 of 4 survive cancer. The prognosis for patients diagnosed with cancer has improved significantly over the last decades, where the 75% survival rate is twice as high as it was 50 years ago [2]. Although an improvement, the prognosis is still bleak for some cancer types. For lung cancer, one of the most deadly forms of cancer, 24.7% of males and 31% of females diagnosed are still alive five years after diagnoses [2].

The importance of early diagnosis of cancer cannot be overstated. For lung cancer, again, if the cancer is detected in stage I, 64% of males and 72.8% of females are alive after five years [2].

Cancer is the uncontrolled and unregulated growth and, in some cases, spread of cells. These cells cluster together and form tumors, which can be malignant or benign. Benign tumors are localized tumors which almost always are curable. Malignant tumors are tumors where the cells have a metastatic potential, meaning the cells can invade the blood or lymph flow and migrate to distant sites in the body to form secondary tumors.

In addition to migratory properties, cancer cells seem to divide for infinity. Where

regular cells have mechanisms which trigger *apoptosis*, programmed cell death, when the cell has divided a certain number of times (50-60 in culture for human fibroblasts), cancer cells seem to evade this mechanism [3]. The cervical cancer cells of Henrietta Lacks, for instance, have been dividing for 50 years, more than 20 000 times [3].

The progression of cancer is commonly divided in 4 or 5 stages (0-IV). The characteristics of stage 0 cancer is a localized tumor, meaning the cancer has not yet spread to nearby tissue. Cancer detected in stage 0 is almost always curable. Cancer in stage I has spread to nearby tissue but has not yet penetrated deeply into the tissue. Cancer in stages II and III is characterized by tumors being embedded deeply inside into nearby tissue and some cancers have at this stage spread to the lymph nodes of the patient. The last stage, stage IV, is characterized by metastasis and formation of secondary tumors in other organs [4].

Measuring the deformability or stiffness of cells, meaning a cells willingness to change shape as a response to external mechanical forces has been shown to be a promising label-free biomarker for disease. Several diseases have been linked to a change in mechanical characteristics of cells, among them sickle cell anemia. In sickle cell anemia, a single-nucleotide polymorphism in the β-globin gene leads to substitution of valine for glutamic acid in the β-globin chain. Following deoxygenation, the mutated hemoglobin molecules polymerize to form bundles. The polymer bundles result in erythrocyte sickling, which in turn results in impaired rheology of blood and aggregation of blood cells, leading to vaso-occlusion or stasis of blood. The blood rheology is dictated in part by the plasma viscosity and erythrocyte deformability. After polymerization of hemoglobin, the erythrocytes become less deformable and can become mechanically sequestered leading to vaso-occlusion [5]

Kubankova et al. performed studies of mechanical properties of blood cells during and after COVID-19 infection and found a significant change in deformability and size for various blood cells, and in some cases the change in deformability lasted for months after the infection was over. More specifically, it was reported an increase

in deformability of peripheral blood lymphocytes for patients with severe COVID-19. In addition to this they discovered changes in neutrophil size and deformability [6].

Over the last decades, a change in deformability of cells from different cancer types has been recorded. Various single-cell techniques have been applied to assess the deformability of cancer cells, such as optical stretching and micropipette aspiration [7, 8]. Lekka et al. performed single-cell measurements of three cancerous cell lines and two normal ones with a scanning force microscope and found one order of magnitude difference in Young's modulus between malignant and non-malignant cells, with normal cells having the higher Young's modulus [9]. Subsequently, Lekka et al. again published a more in depth study, and using AFM found independently of cancer type, for bladder, melanoma, prostate, breast and colon cancer, the cancer cells have a lower Young's modulus than their non-malignant counterpart [10].

Although the results from single-cell studies are promising, they are time consuming (around 10-100 cells/hour). A high-throughput method for mechanoprofiling is a promising solution to this problem. Using a microfluidic approach, one could ascertain deformability by measuring entry times and transit times through a narrow constriction for hundreds or thousands of cells per second.

Studies on neutrophils, which are known to stiffen when exposed to inflammatory mediators such as N-formyl-methionyl-leucyl-phenylalanine (fMLP) or Tumor Necrosis Factor-α (TNF-α), have been conducted by Rosenbluth et al. They used a microfluidic constriction device to measure the transit time. When neutrophils were exposed to fMLP, they had a higher transit time than their normal control neutrophils, showing that the technique has viability for detecting changes in stiffness [11].

Graybill et al. used a microfluidic constriction deformation channel to analyze the Young's modulus of healthy astrocytes and astrocytoma cells of grade II-IV. The researchers measured entry time, transit time and elongations of cells and used finite element analysis (FEA) and a neural network to assess the stiffness of single

cells. They did not find a strong correlation between increasing malignancy of astrocytomas and decreased Young's modulus using this method [12].

Although not all microfluidic approaches are able to distinguish between cell stiffness, this might be due to some cells not having altered mechanical phenotype for disease. The amount of research is vast, and much is still unknown. However, based on the successes and potential benefits, a microfluidic approach for characterizing changes in mechanical phenotypes seems like a viable next step in disease and cancer diagnosis.

The aim of this work is to develop a protocol for realization and application of microfluidic constriction devices, and to asses the viability of discrimination between malignant and non-malignant urinary bladder cells based on transit time of the cells through the constriction region.

Chapter 2

Theory

2.1 The Cytoskeleton

Cells are building blocks for life, the basic unit of biology. Every organism is either single-celled or made up of cells. Generally, cells are separated in two different categories: eukaryotes and prokaryotes. In general, prokaryotes have a less complex structure than eukaryotes. The genetic material of a prokaryote is suspended in the cytosol, where eukaryotes have a nucleus containing the organisms genetic material [13].

The cytoskeleton is a complex structure of closely linked proteins which serves as the skeleton of cells, as well as a molecular highway for transport across the cell. Diffusion is only effective for shorter distances; transport over large distances in the cell is therefore dependent on active transport through molecular motors. The cytoskeleton is comprised of three different types of proteins, which are working together to maintain the structural integrity of the cell.

The smallest part of the cytoskeleton is the microfilament, also called the actin filament. The microfilament has a diameter of 7 nm and has various functions in the cell. One of the most studied functions of the microfilament is its role in muscle contraction, where actin and myosin work together to create tension in muscles.

Microfilaments can also assemble in a tight bundle and serve as microvilli, or as a less regular collection of filaments in the cellular cortex. The actin cortex consists of filaments which lie directly below the cellular membrane and maintains the outer structural integrity of the cell [9]. The microfilament also plays a key role in cell locomotion, cell division and phagocytosis.

The microfilament is composed of polymerized actin. Actin is an abundant protein found in most eukaryotic cells, and is commonly found in the globular form, called G-actin. G-actin binds a Mg^{2+} ion which can be complexed with either ATP or ADP. When ATP or ADP binds to G-actin, it initializes polymerization of G-actin into F-actin filaments, which in turn will coil and create a double helix structure. ATP-bound G-actin will preferentially add to one end of the filament, denoted the (+) end, giving the filament an inherent polarity. Once the G-actin has been incorporated into the F-actin, the bound ATP is hydrolysed [3].

The second key protein of the cytoskeleton is the microtubule. Microtubules are stiff structures where a single microtubule can extend up to 20 µm, and they have diverse roles in the cell, involving transport, movement of organelles and mitosis among others. Microtubules can, like actin, bundle together to create specialized structures such as cilia and flagella. Microtubules are formed by two sub-units, α- and β-tubulin. Both sub-units can bind to one molecule of GTP and added preferentially to one end of the polymerizing microtubule, also denoted the (+) end. Microtubules are composed of 13 laterally associated protofilaments, which then form the microtubule itself with a diameter of around 25 nm.

The microtubules can associate with each other in several, ways creating doublets (two microtubules) and triplets (three microtubules). The doublets and triplets are mostly found in specialized structures such as cilia and flagella, as well as centrioles and basal bodies [13].

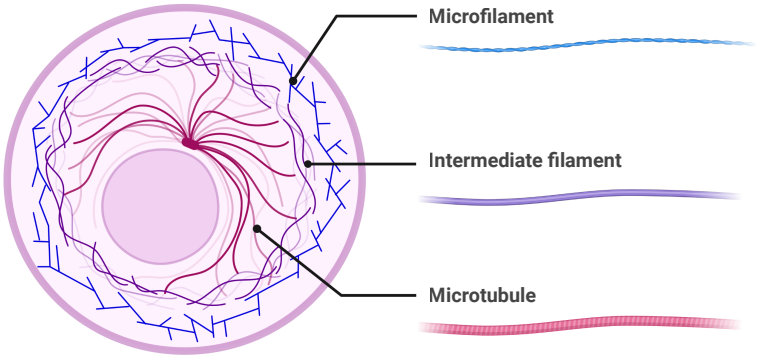

Figure 2.1: Illustration of the cytoskeleton, where microfilaments (actin filament) are colored blue, intermediate filaments purple and microtubules red. Figure made with BioRender.

The third main component of the cytoskeleton is the intermediate filament. The size of the intermediate filament lies between the microfilament and the microtubules, with a diameter of about 10 nm. Intermediate filaments have great tensile strength and are able to withstand a significant amount of stress and strain. With this ability, they serve as the cells primary scaffold, endowing cells with structural integrity. In opposition to microtubules and microfilaments, intermediate filaments do not have innate polarity, and as such they are not used for cargo transport by molecular motors. Intermediate filaments do, however, have several key roles in the cell. In addition to providing the cell with structural integrity, they are involved with the formation of the nuclear lamina and strengthening of nerve cell axons [3, 13]. An illustration of the cytoskeleton can be seen in Figure 2.1

Together, the microfilament, intermediate filament and the microtubules serve as the cytoskeleton of the cell.

The cytoskeleton extends from the nucleus of the cell through nucleo-cytoskeletal coupling. The coupling of these components is thought to be a protective measure to maintain the structural integrity of the nucleus during deformation, as large deformation of the nucleus may cause damage to DNA. Wang et al. performed studies decoupling the cell membrane, cytoskeleton and nucleus in order to study

the interaction between the components on the deformability of the nucleus. The decoupled elastic modulus of the cell membrane, cytoskeleton and nucleus was found to be 2.90 ± 0.04 kPa, 4.28 ± 0.33 kPa and 2.01 ± 0.10 kPa, respectively. Measurements of the elastic modulus of the nucleus when coupled with the cytoskeleton was almost double that of the decoupled nucleus, with an elastic modulus of 3.81 ± 0.21 kPa [14].

2.2 Cancer

Cancer is a deadly and common disease and is generally arise from mutations in an organisms genetic material, leading to uncontrolled differentiation and avoidance of apoptosis. Cancers form tumors which can be benign or malignant, where benign tumors are localized tumors which rarely are deadly. Malignant tumors are cancers which metastasize and form secondary tumors.

Studies have been conducted on the cytoskeletal changes occurring in the later stages of cancer. Wang et al. compared the elastic modulus of the nucleus of early stage cancer cells RT4 cells with late stage T24 cells and found that the nucleus of T24 exhibit a lower elastic modulus, due to T24 cells having a lower density of cytoskeletal proteins. After anti-cytoskeletal drug treatment with cytochalasin D and nocodazole, the researchers found no significant difference in nuclei stiffness between RT4 and T24 cells [14].

2.2.1 Pathogenesis of Cancer

Generally, cancer has been linked to mutations in two broad classes of genes: proto-oncogenes and tumor-suppressor genes. These mutations can arise from exposure to carcinogens, which are cancer promoting substances can be encountered in the environment.

Before mutation, proto-oncogenes promote cell growth and cell division. When

proto-oncogenes mutate they become oncogenes and turn on inappropriately, leading to excessive, unwanted, and uncontrolled cell growth and division.

Tumor-suppressor genes work by restraining cell growth and division, and mutation of these genes can inactivate them leading to unrestrained cell growth and division.

Healthy cells sense external signals which stimulate the cells to divide. By mutation of genes, cancer cells acquire the ability to proliferate without external signaling, and do not register signals that should restrict cell division.

Initially, tumors are hypoxic and need to create new blood vessels to get oxygen, in a process called angiogenesis. Angiogenesis has been linked to metastatic ability, where a high degree of tumor vascularization in the primary tumor increases the tumor cells ability to enter the circulatory system and metastasize [13].

2.2.2 Metastasis

After forming the primary tumor and a blood supply through angiogenesis, some tumors start the process of migration. Between cells, there is a complex network of proteins and polysaccharides called the *extracellular matrix* (ECM). The ECM functions as a biomechanical barrier for cells to pass in order to migrate successfully. For cells to pass through the ECM, they can exhibit one of two migration modes, in a characteristic called *migration plasticity*.

Some cancer cells have the ability to release proteases, which are enzymes that can hydrolyze peptide bonds of proteins, effectively cleaving them. This means that passage through the ECM will be easier when proteases have cleaved proteins of the ECM. The "path-generating" release of proteases is called the mesenchymal mode, and cells in this mode can be characterized by their elongated cell morphology and adherence to the surrounding ECM.

The other mode of migration, called "path-finding" ameboid mode can be observed for cells which do not depend on protease-degradation of the ECM in order to mi-

grate. These cells squeeze through the pores of the ECM and are highly dependent on being deformable and having low adhesion to ECM. The low adhesion to ECM allows cells to move faster than cells in the mesenchymal mode.

The migration plasticity and the transition between mesenchymal and ameboid phenotypes has been found to be highly responsive to cellular signals and changing microenvironment conditions [15, 16].

Once migrating tumor cells has reached a blood vessel, they can begin the process of entering the blood stream in a process called *intravasation*. When the cell has entered the blood stream, it is considered a circulating tumor cell (CTC) and is a potential metastatic seed. The bloodstream is a hostile environment for cancer cells, and very few CTCs reach their destination to form a secondary tumor [17].

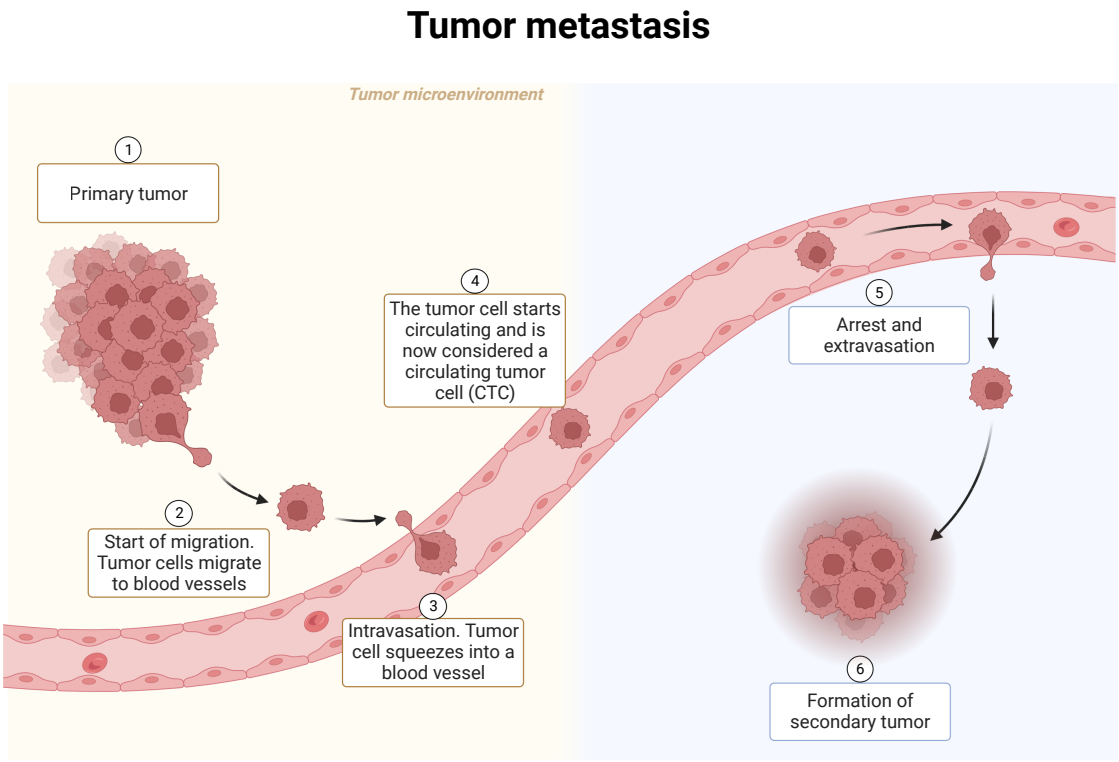

Figure 2.2: Illustration of the metastatic cascade. Tumor cells from a primary tumor starts migration to a newly formed blood vessel. During intravasation the cell enters the blood stream and starts to circulate. Arrest and exiting in a process called extravasation, before forming a secondary tumor. Figure made with BioRender.

2.3 Microfluidics

Microfluidics, a field of study involving fluid flow induced by external forces in devices with dimensions in the microscale, has been an active field of study for several decades. There are multiple reasons for scaling down to the microscale when working with fluids. Some of them being the amount of sample needed is radically reduced. In addition, shorter reaction times, possibilities for parallel operations, they also allow for integrating an entire laboratory onto a single chip, i.e., lab-on-a-chip (LOC) [18, 19].

A fluid is characterized by the ability to change shape determined by the vessel containing it. In a fluid, a small shear force will lead to a large change in relative position of the atoms in the fluid [19]. When the forces acting on the fluid cease, the atoms will not necessarily return to their original position, and the fluid not the initial shape. Terminology like incompressible and compressible fluids will be used briefly for defining the use case of the Navier-Stokes equation. An incompressible fluid, is a fluid where the mass density (ρ) of an infinitesimal volume element does not change while the volume element moves along the flow, meaning that the mass density of the fluid is constant in space and time [19, 20].

The continuum hypothesis states that the macroscopic properties of a fluid are the same as if the fluid was perfectly continuous. The continuum hypothesis is assumed to be correct for the following theory, and the fluid in this thesis are treated as a continuum.

2.3.1 Governing Equations

The following section is largely based on Henrik Bruus' *Theoretical Microfluidics*, for a more in-depth explanation and derivation of equations, the reader is directed to the original text [19].

Fluids are classified as either Newtonian or non-Newtonian. The distinguishing

factor between these fluids is the rate of deformation as response to viscous stress present during flow. For Newtonian fluids the viscous shear stress τ (Equation 2.1) is proportional to $\frac{\partial v}{\partial y}$, i.e. the derivative of the velocity in the direction of flow and perpendicular to the shear plane, where η is the viscosity [20].

$$\tau = \eta \frac{\partial v}{\partial y} \tag{2.1}$$

A common method of characterizing a flow regime in microfluidics is by assessing Reynolds number (Re) (Equation 2.2). Reynolds number is a dimensionless number that describes the fluid regime, either as turbulent or laminar. Turbulent flow is a chaotic flow regime, where predicting the position of a particle as a function of time is impossible. Turbulent flow can be desired when mixing two fluids [18].

Laminar flow is defined as a flow where a particles position in the fluid can be predicted as a function of time. In laminar flow, no mixing occurs between laminar streams, except for the diffusion between streams. Mixing two fluids with a laminar flow regime is therefore quite slow [18].

Reynolds number is defined as

$$Re = \frac{\rho v D_h}{\eta}, \tag{2.2}$$

where ρ is the fluid density, v is the characteristic velocity of the fluid, η is the fluid viscosity and D_h is the hydraulic diameter.

Generally, a Reynolds number lower than 2300 indicates a laminar flow and higher implies a turbulent flow regime [18].

To describe movement of a fluid, Navier-Stokes equation (Equation 2.4) is commonly used. Simplifications and boundary conditions enable analytical solutions to be expressed for idealized systems. The no-slip boundary condition states that movement of a fluid is zero at the boundaries (channel walls), or more precisely

$$v(\mathbf{r}) = v_{wall}, \text{ for } r \in \partial\Omega. \tag{2.3}$$

Equation 2.3 states that the velocity of the fluid flow at the boundary $\partial\Omega$ is the same as the velocity of the wall. As the wall is stationary, the velocity of the fluid field at this point is zero.

The Navier-Stokes equation is given as

$$\rho(\partial_t \mathbf{v}) + (\mathbf{v} \cdot \nabla)\mathbf{v} = -\nabla p + \eta\nabla^2\mathbf{v} + \mathbf{f}_{body} \tag{2.4}$$

where v is the fluid velocity, p is the pressure, ρ is the fluid density, η is the viscosity of the fluid, f_{body} is the sum of the external forces, i.e. gravitational and electrical. The Navier-Stokes equation combines inertial forces, pressure forces, viscous forces and external forces in one equation, where the left-hand side of the equation denotes the inertial forces of the fluid, $-\nabla p$ denotes the pressure forces, $\eta\nabla^2\mathbf{v}$ the viscous forces, and the external forces f_{body}. f_{body} can alternatively be written as

$$\mathbf{f}_{body} = \rho g + \rho_{el}\mathbf{E}, \tag{2.5}$$

where ρ is the density of the fluid, g is the gravitational acceleration, ρ_{el} is the charge density and $\boldsymbol{E}$ is the external electric field density.

For an incompressible, Newtonian fluid, the divergence of the velocity field will be zero ($\nabla v = 0$), simplifying Equation 2.4 to

$$\rho\partial_t \mathbf{v} = -\nabla p + \eta\nabla^2\mathbf{v} + \mathbf{f}_{body}. \tag{2.6}$$

For a steady-state, pressure driven system, called *Poiseuille flow*, further simplifications are possible. A steady-state implies a constant fluid velocity, meaning $\partial_t \mathbf{v} = 0$, and gravitational forces are neglected, which results in Equation 2.6 be-

coming

$$\nabla p = \eta \nabla^2 v. \tag{2.7}$$

The Navier-Stokes equation is in this form just named Stokes equation. Stokes equation can be solved analytically for flow in various geometries, such as channels with circular, ellipsoid, and rectangular cross-sections.

For a circular channel with channel length L and radius a, the fluid velocity can be expressed as

$$v_x(y,z)_{circular} = \frac{\Delta p}{4\eta L}(a^2 - y^2 - z^2). \tag{2.8}$$

The flow through the channel is in positive x-direction, z denotes the height coordinate in the channel and y represents horizontal axis, both bounded by the radius of the channel, i.e. $-a < y, z < a$.

The flow rate, Q, that is, the rate of fluid passing through the channel per unit of time, can be gathered by integrating the velocity field function over the cross-sectional area,

$$Q \equiv \int_C v_x(y,z) dy dz. \tag{2.9}$$

Using Equation 2.9 and Equation 2.8, the flow rate for a circular channel can be derived and is given as

$$Q_{circular} = \frac{\pi a^4}{8\eta L}\Delta p. \tag{2.10}$$

The velocity field for a Poiseuille flow in a rectangular channel is given as

$$v_x(y,z)_{rectangular} = \frac{4h^2 \Delta p}{\pi^3 \eta L} \sum_{n,odd}^{\infty} \frac{1}{n^3} \left[1 - \frac{cosh(n\pi \frac{y}{h})}{cosh(n\pi \frac{w}{2h}} \right] sin(n\pi \frac{z}{h}). \tag{2.11}$$

Again, using Equation 2.9 and Equation 2.11, the flow rate of a rectangular channel

can be expressed as

$$Q_{rectangular} \approx \left[1 - 0.63\frac{h}{w}\right]\frac{h^3 w}{12\eta L}\Delta p. \tag{2.12}$$

where h is the height of the channel, w the width and L the length.

For Poiseuille flow, the relations can be summarized in the Hagen-Poiseuille law

$$\Delta p = R_{hyd}Q = \frac{1}{G_{hyd}}Q. \tag{2.13}$$

Where R_{hyd} and G_{hyd} are proportionality factors which are know as the hydraulic resistance and hydraulic conductance, respectively.

For a circular channel, the hydraulic resistance is given as

$$R_{hyd,circle} = \frac{8}{\pi}\eta L\frac{1}{a^4}. \tag{2.14}$$

Where η is the viscosity, L the length of the channel and a the radius of the channel. Likewise, the hydraulic resistance for a rectangular channel can be expressed as

$$R_{hyd,rectangle} = \frac{12\eta L}{1 - 0.63\frac{h}{w}}\frac{1}{h^3 w}, \tag{2.15}$$

where h is the height of the channel and w the channel width.

For a channel with a square cross-section, hydraulic resistance is

$$R_{hyd,square} = 28.4\eta L\frac{1}{h^4}. \tag{2.16}$$

Hagen-Poiseuilles law (Equation 2.13) is analogous to Ohm's law, and series and parallel hydraulic resistors are analogous to resistors in series and parallels in a electric circuit, where hydraulic resistors in series is expressed by [19]

$$R = R_1 + R_2. \tag{2.17}$$

And similarly, the resistance of parallel resistors can be expressed as

$$R = (\frac{1}{R_1} + \frac{1}{R_2})^{-1}. \tag{2.18}$$

2.4 Mechanics

When forces alter the shape of a material, either permanently or temporarily, the deformation caused is called *strain*. The forces which cause the strain are called *stress*.

For relatively small deformations, the mechanical behavior at low temperatures may be elastic, meaning it conforms to Hooke's law

$$\sigma = E\epsilon, \tag{2.19}$$

where E is the modulus of elasticity, often called Young's modulus, ϵ is the strain. From Equation 2.19 it follows

$$\frac{Stress(\sigma)}{Strain(\epsilon)} = E. \tag{2.20}$$

Hooke's law has a limited range of validity. During an elastic deformation, the deformation is reversible, meaning that once the load is removed the deformed object regains its original shape and the energy put into the material from the stress is recovered. All materials have an *elastic limit*, from which if stress continues to increase, the material will *yield* and not return to the original form. Following the elastic limit, plastic deformation occurs. A plastic deformation is irreversible; when the stress is removed, the material does not return to its original shape and the energy is lost [21].

One form of stress forces is called *shear*. During shearing, the faces of an object are being forced in different directions. This is represented by the shear-stress equation

(Equation 2.21).

$$\sigma_{shear} = \frac{F_{\parallel}}{A}, \tag{2.21}$$

Where $F_{\parallel}$ denotes a force acting parallel to the face of the material, and A the area of displacement.

Shear stress leads to a shear strain which can be represented by

$$\epsilon_{shear} = \frac{x}{h} \tag{2.22}$$

Where x is the displacement resulting from shearing and h is the distance between shear planes.

2.4.1 Viscosity

Viscosity, the internal friction of a fluid, is an important parameter to consider when working with fluids. Viscous forces oppose the motion of one portion of fluid relative to another. Fluids which flow readily, such as water have low viscosity, and fluids which flow slowly have higher viscosities, e.g. honey.

2.4.2 Viscoelasticity

When a material has both viscous and elastic characteristics, it is described as viscoelastic. For relatively small deformations, the mechanical behaviour following deformation may be elastic and described by Hooke's law (Equation 2.19).

Elastic deformation is instant. The deformation occurs the instant stress is applied, and the deformed object returns to its original shape the instant the stress is released. Viscous deformation is gradual over time in response to applied stress. A completely viscous deformation is not reversible; the deformed object has no

structural memory and will therefore not regain its original shape after stress is released [22].

A number of viscoelastic materials are susceptible to *creep*. Creep is a time-dependent deformation occurring when the stress level is kept constant. Creep can be represented by the creep modulus, defined as

$$E_c(t) = \frac{\sigma_0}{\epsilon(t)}. \tag{2.23}$$

Kollmansberger and Fabry [22] inform that cells exhibit creep and stress relaxation which follows a power-law response. Power-law behavior can be explained through creep experimentation. Kollmansberger and Fabry, again, explain it as loading a material at time $t = 0$ with constant force F and the material deformation d versus time is recorded. The ratio of $d(t)/F$ defines the creep function as

$$J(t) = d(t)/F = j_0 \cdot (t/\tau_0)^{\beta} \tag{2.24}$$

where j_0 denotes the compliance of the material, time is normalized by a timescale τ_0 and β is the power-law exponent. If β approaches unity, Equation 2.24 simplifies to

$$d/F = j_0 \cdot t$$

which is Newton's law for viscous deformations.

If β approaches zero, Equation 2.24 simplifies to

$$d/F = j_0$$

which is equivalent to Equation 2.19, Hooke's law for elastic deformations.

2.5 Deformation Cytometry

Measuring the properties, characteristics or number of cells is termed cytometry, and can either be single-cell methods such as micropipette aspiration, optical stretching, parallel plate rheology or atomic force microscopy [23]. These methods are low throughput, meaning that a small number of cells per unit of time can be measured. One high throughput cytometry method is flow cytometry, where cells are guided in a single file through a laser light, forward scattering and backward scattering are measured and information regarding size, granularity and fluorescence can be obtained. Flow cytometry cannot, however, detect mechanical properties of cells.

A change in mechanical properties of a cell has been linked to the pathophysiology of various hematologic diseases such as sepsis, diabetic retinopathy and sickle cell anemia, among others [11]. And, as stated in Section 1, mechanical properties may serve as a label-free biomarker for high-throughput analysis of cells to discover various diseases. Deformation cytometry is a cell cytometry method where the general aim is to discover cell characteristics by the deformation of cells. The deformation scheme can be separated in three categories: constriction deformation cytometry (cDC), shear deformation cytometry (sDC) and extensional flow deformation cytometry (xDC) [23]. The differences between the three schemes can be seen in Figure 2.3 and is detailed below.

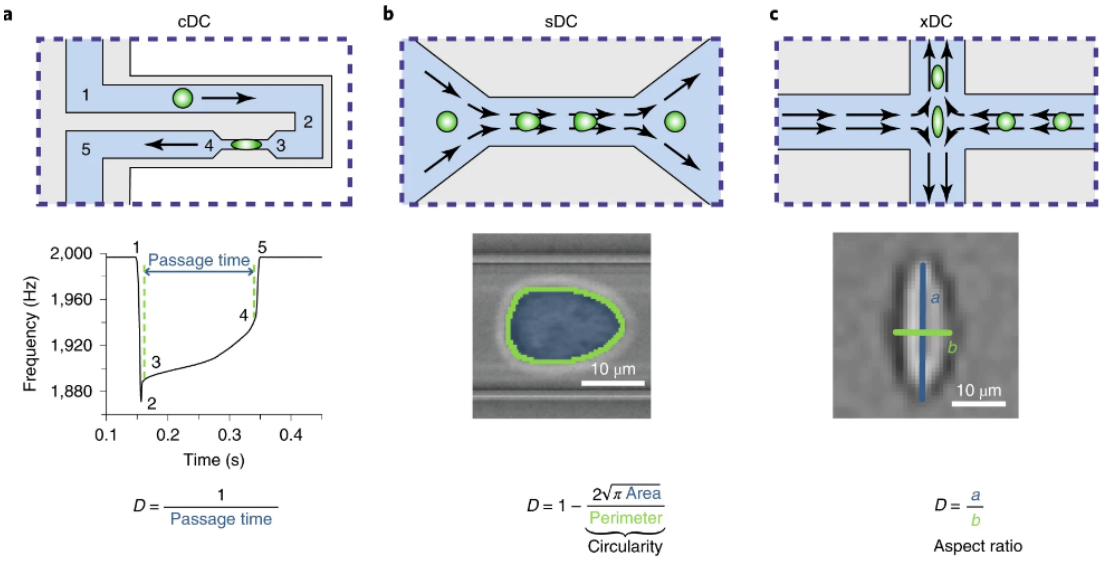

Figure 2.3: Schematic illustration of cDC (a), sDC (b) and xDC (c). With D, the deformability parameter represented below each deformation scheme. Adapted with permission from [23].

Constriction deformation cytometry (cDC) measures the time cells use to pass a constrictive region of a microfluidic channel. The channel in the constriction region has smaller cross-section than the relaxed cell diameter of the cells being pushed through, meaning that the cells are in contact with the channel wall during the passage through the constriction. Measurement of time can be performed through optical observation and recording, electrical resistance measurements or mechanical frequency changes using a suspended microchannel resonator (SMR) [23]. The time it takes for cells to pass the constriction, termed the *transit time*, can be related to the elastic modulus of the cell. When a cell is deformed inside the channel, the area of the cell in contact with the channel walls will generate a normal force and a friction, which will influence the time it takes for the cell to transit. The size of the normal force will vary with cell size and Young's modulus of the cell [24].

The two other deformation schemes use fluid flow to deform cells. Shear deformation cytometry (sDC) imposes a shear stress on the object being deformed by hydrodynamic flow and extensional flow deformation cytometry (xDC) uses an extensional flow, which can be created by a junction in the microfluidic channel with opposing fluid flow directions.

Chapter 3

Materials and Methods

This chapter outlines the scientific methods and materials used for all experimental work performed as part of this thesis. The cell culture work detailed in Section 3.2.2 and Section 3.2.1, apart from incubation, was performed in a sterile environment. Microfabrication conducted to realize microfluidic devices, described in Section 3.1.2 and Section 3.1.3 was performed in a cleanroom environment (ISO5 and ISO7) and at room temperature. Some of the methods described here were initially performed by the author during the fall semester of 2022, as a part of the Nanotechnology Specialization Project. The description of these methods will therefore be similar to the authors description in the final report of the Nanotechnology Specialization Project [25].

3.1 Fabrication of Constriction Devices

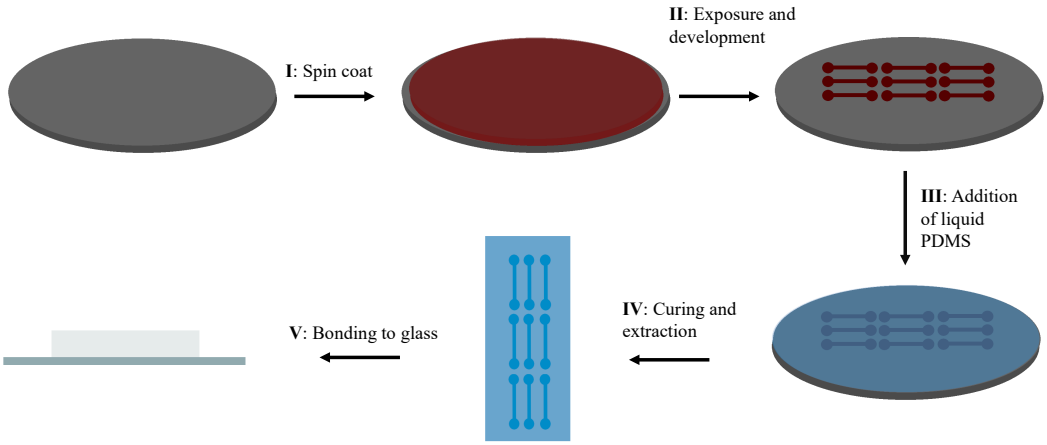

Figure 3.1: Schematic illustration of the process steps for photolithography and soft lithography. The process starts with a cleaned silicon wafer, which is spin coated with a photoresist (I) and patterned with a UV light source (II). Liquid PDMS is then poured over the hardened pattern on the wafer (III), and subsequently cured (IV). The cured PDMS forms a spatial negative of the pattern on the wafer, and can be mounted on a glass slide both to be observed and to yield a microfluidic device (V).

Microfluidic devices can be fabricated with various techniques, one of the most common being a photolithography process followed by a soft lithography process, illustrated in Figure 3.1. Photolithography consists of coating a silicon wafer with a photosensitive polymer-resin referred to as a photoresist and irradiating the photoresist with the intended pattern. This allows for creation of micro- to nanostructures. The exposed photoresist can subsequently be used in a soft lithographic process, where polydimethylsiloxane (PDMS), a curable polymer, can be poured over the wafer. Polydimethylsiloxane is cured under elevated temperatures, and will form a spatial negative of patterned photoresist. Inlets and outlets can be punched and the PDMS can be mounted on a glass slide, allowing for easy observation of fluid and cell behavior through the glass slide.

3.1.1 Channel Design

The original design intended for the microfluidic channel was provided by Kartik Totlani. Some changes were made from the original design, and the work on the channel design was mainly implemented in CleWin 4 [26]. The original design had pillars to support the roof of the finished PDMS device. These pillars were found to be obsolete, and even a detriment to the movement of cells in the channel and were thus removed. In addition, the constriction region of the channel was initially 130 µm in length but was later elongated to 300 µm. All cell experiments in this thesis were conducted with a pillar-less microfluidic device with a 300 µm long constriction region. The entire mask for the devices is intended for a 4-inch silicon wafer, and contains three rows of 24 channels, divided into 6 columns, giving 72 channels per soft lithography cycle. The channels are divided into sections of 3 x 4 channels, which has been found to fit appropriately to a 26 mm x 76 mm cover slide.

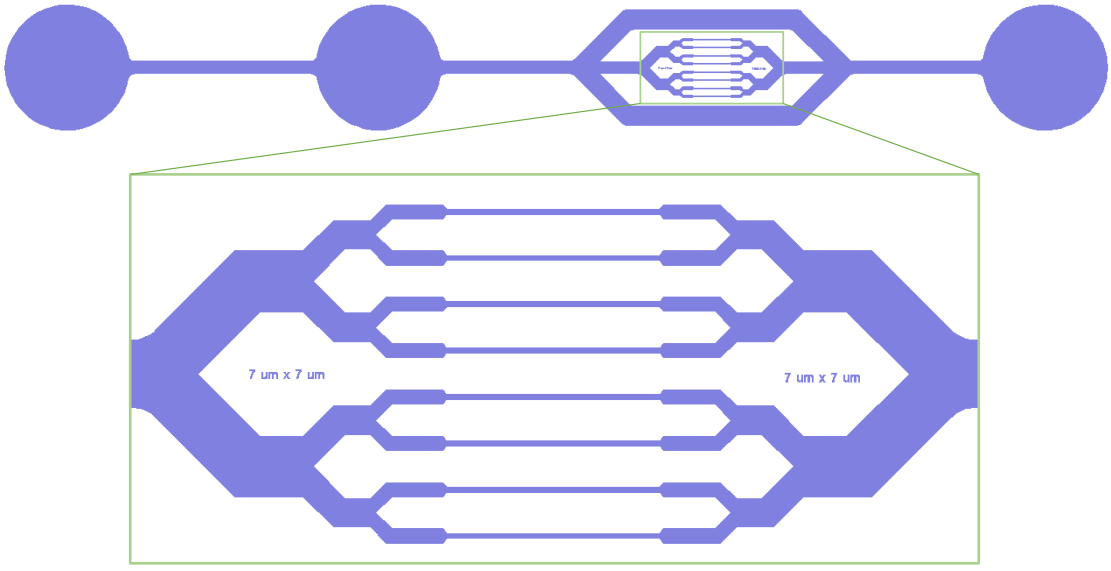

Figure 3.2: The mask used for fabrication of masters for microfluidic devices with 7 x 7 µm^2 constriction cross-sectional area. The 10 x 10 µm^2 mask is equivalent, with 10 µm constrictive channel width and height.

Each device was designed with two inlets and one outlet. This was realized to

attain the ability to dilute concentration of cells while performing experiments. To dilute the cell concentration, one inlet can be connected to a syringe with PBS and one with the cell suspension. Adjusting flow rates would allow fine-tuning of the effective concentration.

After the inlets, a primary bifurcation is placed which serves as a bypass channel in order to maintain constant pressure over the constrictive region and allow most cells to pass outside the constrictive region. This is also intended to limit the pressure changes on other constriction channels when one of the eight constriction channels is occupied by a cell. Three more bifurcations follow, and for each bifurcation, the width of the channel halves until the width is 20 µm, before a sharp reduction in width leads to the constrictive part of the channels, as seen in Figure 3.2.

Two different masks were used for cell experiments in this thesis. The channels are identical apart from the constrictive region width and the channel height. The first channel used has a 7 µm wide constrictive region and a channel height of 7 µm. The second channel has a constrictive region width of 10 µm and a channel height of 10 µm.

3.1.2 Photolithography

A 4-inch silicon wafer was prepared in a solvent bath of acetone for three minutes under gentle agitation. After 3 minutes, the wafer was extracted from the acetone bath while continuously flushed with isopropyl alcohol (IPA) to not allow any acetone to dry on the surface of the wafer, as this creates an undesirable film over the wafer. Following the solvent clean, to remove organic contaminants, a UV ozone treatment (30 °C, 3 minutes, Novascan Technologies Design) was performed on the wafer.

Following the UV ozone treatment, a dehydration bake step was performed (180 °C, 20 minutes, Süss MicroTech), to ensure proper dryness of the wafer surface. This was done to improve adhesion between the wafer surface and the photoresist.

For this thesis work, two different channel heights were used. A channel with 7 µm height and a 7 µm constrictive width was fabricated with the mask design seen in Figure 3.2, and an equivalent channel with 10 µm height and 10 µm constriction width. The process parameters for both channels are the same, except for the spin speed.

For the wafer with the 7 x 7 μm^2 constriction cross-sectional area, a spin speed of 2200 RPM was found to be appropriate. The spin was conducted in a three-step process, first depositing the mr-DWL 5 (micro Resist technology GmBh) with a Pasteur pipette in the middle of the wafer surface. mr-DWL 5 is a viscous photoresist and moving the wafer vertically and allowing the photoresist to spread over most of the wafer surface was found to be beneficial for the quality of the coat. The wafer with the deposited photoresist was then accelerated with an acceleration of 500 RPM/s, until it reached 2200 RPM. The wafer was then spun at 2200 RPM for 30 seconds and subsequently decelerated and stopped.

For the channel with a 10 x 10 μm^2 constriction cross-sectional area, the process steps remained identical, except for the spin speed which was set to 1500 RPM.

For this resist, a soft bake prior to exposure is necessary. This was performed in a programmable oven (Süss MicroTech) and conducted for 50 °C for 2 minutes, and gently ramping the temperature up to 90 °C by 9 °C per minute, then baking at 90 °C for 4 minutes.

The wafer was exposed in a MLA 150 (Heidelberg Instruments), with an exposure dose of 320 mJ/cm^2 and a wavelength of 405 nm. Following exposure, a post-exposure bake was performed. Again, conducted in an oven (Süss MicroTec) for 50 °C for 2 minutes, ramping up to 85 °C by 8 °C per minute, baked at 85 °C for 6 minutes and gently cooled to 40 °C by reducing the temperature by 2 °C per minute.

Development of the photoresist was performed under constant, gentle agitation in the organic solvent-based developer mr-Dev 600 until completely developed, which took approximately 7 minutes. Following development, the wafer was submerged

in isopropyl alcohol, and dried with nitrogen (N_2) gas.

To ensure proper development, the structure in photoresist was inspected in a yellow light microscope (Eclipse LV150, Nikon) with a 5X and 10X objective, checking that no unwanted photoresist remained on the wafer surface, as well as checking channel edges for signs of over-development.

To gauge the height of the patterned photoresist, a stylus profilometer (Dektak 150, Veeco) was used. The profilometer has a tip (12.5 µm) which moves across surfaces, and while in contact, discovers height changes on a surface. The profilometer test was conducted for several channels over different regions of the same wafer, to ensure homogeneity of the channel height across the wafer.

3.1.3 Soft Lithography

The first step of the soft lithography process is to silanize the master to decrease the adhesion between the patterned photoresist and the PDMS, making it easier to peel out when cured. This was performed by placing the wafer in a 6-inch polystyrene Petri dish, with the patterned side up and depositing a few drops of fluorosilane ((1H, 1H, 2H, 2H-perfluorooctyl)trichlorosilane) in a glass vial and leaving the vial and the wafer inside a desiccator under vacuum for 15 minutes.

Polydimethylsiloxane pre-polymer (Sylgard 184, Dow) was mixed with a curing agent in a 10:1 ratio. 90 g of PDMS and 9 g of curing agent was found to be appropriate for a 6-inch Petri dish. The curing agent and PDMS pre-polymer is mixed in a plastic cup for approximately 5 minutes. The mixing creates substantial gas bubbles in the PDMS. As bubbles can destroy a microchannel design, they were removed by placing the plastic cup with the PDMS inside a desiccator under vacuum. The time it takes for completely removing bubbles is weight dependent, and approximately 70 minutes for 100 g of PDMS.

When the PDMS was free of gas, it was gently poured over the freshly silanized wafer in a Petri dish, and cured (65 °C, 4 hrs). Following the curing, the PDMS

slab with the replicated channels from the master was extracted from the Petri dish by first cutting around the design, and gently lifting the PDMS slab. Inlets and outlets were punched with a 1 mm hole puncher, and the microfluidic device was covered with scotch tape to limit the amount of dust and contamination entering the channels.

The channels were mounted on glass slides using oxygen plasma activation (100% generator power, 100% oxygen concentration, 2 minutes 30 seconds, Diener Electronics Plasma Cleaner) on both the PDMS and glass slides. After plasma activation, the PDMS is placed on the glass slides quickly and firmly.

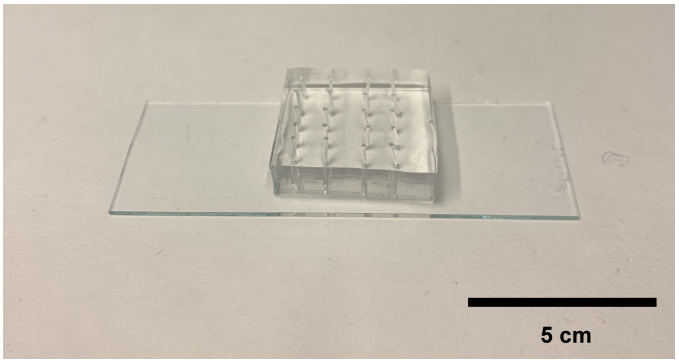

Figure 3.3: Image of a fabricated microfluidic device used for cell experiments.

After bonding the PDMS to glass, another heat treatment was performed, to ensure good bonding between the PDMS and glass, at 65 °C for at least 4 hours. The final microfluidic chip used for cell experiments can be seen in Figure 3.3.

3.2 Cell Culture

Cells from the human cell line T24 (transitional cell carcinoma) and the human cell line HCV29 (non-malignant bladder epithelial cell) were used for experiments with cells. The T24 cell line was established from the bladder of a female patient in 1973. HCV29 is used for comparison as it is a non-malignant bladder cell line, meaning the cells do not metastasize. The cells were cultured at 37 °C in 5% CO_2, in the medium RPMI 1640 (gibco) with 10% fetal bovine serum (Sigma-Aldrich)

and 4 mL L-glutamine (Sigma-Aldrich).

3.2.1 Maintenance of Cells

Two sizes of culture flasks (Avantor) were used. The T25 culture flask has a 25 cm^2 area available for cells to attach, while the T75 has a 75 cm^2 area. The T25 flasks were mainly used for experiments, as confluence was reached quite fast. Generally, cells were seeded according to when experimental activity was planned, i.e., high in T25 flasks if experiments were planned in the coming days and low in the T75 flasks if no experiments were planned. For the T25 flasks, a cell number of approximately 25 000 - 250 000 cells were used to seed. For the T75 flasks, generally, 250 000 - 1 000 000 cells were sufficient.

Along with the cells, 7 mL of cell medium was added to the T25 flasks, and 14 mL of cell medium was added to the T75 flasks. Cell medium was replenished every other or every third day, depending on the number of cells initially seeded. If a low number of cells were seeded, cells could go longer between replenishment of the cell medium.

When confluence was reached, the old media was removed. The adhesion layer of cells was flushed with 5 mL phosphate-buffered saline (PBS) to ensure complete removal of media as this can negatively impact the effect of trypsin. 2-3 mL of trypsin/EDTA (0.25% / 0.02%, Sigma-Aldrich) was added, and the culture flask was placed in a 37 °C room for two minutes. The flask was then agitated, and the effect of trypsinization was observed through a optical microscope (inverted microscope, Nikon) with a 10X objective. If most cells were suspended, the trypsinization was deemed successful.

To stop trypsinization, 8-9 mL of cell media was added to the flask, such that the entire volume, trypsin and cell media was 11 mL. 1 mL of the suspension was extracted in a Pasteur pipette and injected in a Bürker chamber for counting. The rest of the suspension (10 mL) was centrifuged (1200 RPM, 5 minutes, MegaFuge)

while the cells were counted.

After centrifugation, the supernatant was removed, and cell media was added to the centrifuge tube, creating a concentration of approximately 1 million cells per mL cell media. The suspension was seeded in new culture flasks, which were marked with name, cell line, passage number, concentration and date and placed in the incubator.

3.2.2 Preparation of Cells for Experiments

For cells intended for experiments, the cells were extracted from the T25 cell culture flask at $> 80\%$ confluence. The old cell media was removed, the cell culture flasks flushed with 5 mL of PBS and 2 mL of trypsin/EDTA was added to the cell culture flask. The cell culture flask was then placed in a 37 °C room for 2 minutes. After the two minutes, the cell culture flask was given several forceful knocks to ensure detachment of the cells, before observing that the cells had detached in an optical microscope.

If the cells were properly detached, 9 mL of cell media was added to the trypsin/cell solution, to stop the trypsinization process. 1 mL of the solution was extracted in a Pasteur pipette and used for counting in a Bürker Chamber. The rest of the solution was centrifuged (1200 RPM, 5 minutes, MegaFuge). After counting and centrifuging, the supernatant was removed and PBS added to the cells, to make a concentration of approximately 500 000 cells/mL. The cells in PBS were then left in a warm environment (37 °C) for 1 hour before experiments were conducted.

3.2.3 Cell Size

There is limited published data on the cell size of the T24 and HCV29 cell lines, and a general idea of the working cell size is important to decide what channel dimensions to use. To assess the cell size, cells were prepared in a suspension of

PBS with a concentration of 1 million cells per mL of PBS. A high concentration of cells is beneficial for this experiment as it reduces the number of images needed to measure the sizes of a significant number of cells. The cells were prepared as described in Section 3.2.2.

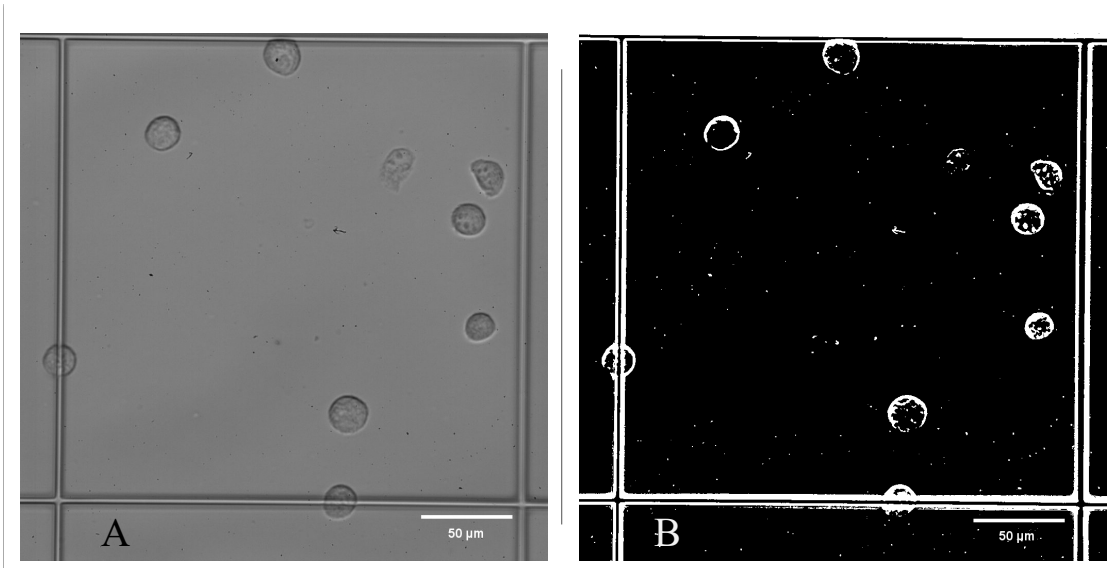

Figure 3.4: **A**: Cells in Haemocytometer with Neubauer improved grid lines. **B**: Binarized image.

After preparing the suspension, 10 µL suspension was injected into one chamber of a C-Chip Disposable Haemocytometer (NanoEnTek, Inc.). The haemocytometer has Neubauer improved grid lines, and the cell size was gathered by collecting images of cells within the grid lines and using the image processing software ImageJ [27] to measure the cell diameters. The image was binarized to easier determine edges of the cells, and 100 cells were measured for each cell line.

3.3 Constriction Experiments

Prior to microfluidic experiments, a bovine serum albumin (BSA, Sigma-Aldrich) and PBS solution was prepared by adding 500 µg BSA to 50 mL of PBS and vortexing until clear. The solution was subsequently used for passivation of the PDMS wall in the microfluidic channel, to limit unwanted effects between the cell

surface and the PDMS wall. After observation of aggregates of BSA inside the devices, the BSA-PBS solution was filtered four times. Firstly, with a 1.2 µm pore size, following a 0.8 µm and twice with a 0.2 µm filter. The BSA solution was aspirated in a Injekt-F Luer Solo 1 mL syringe and injected into the channels. The channel inlets and outlets were then covered with scotch tape and left in room temperature for at least 2 hours.

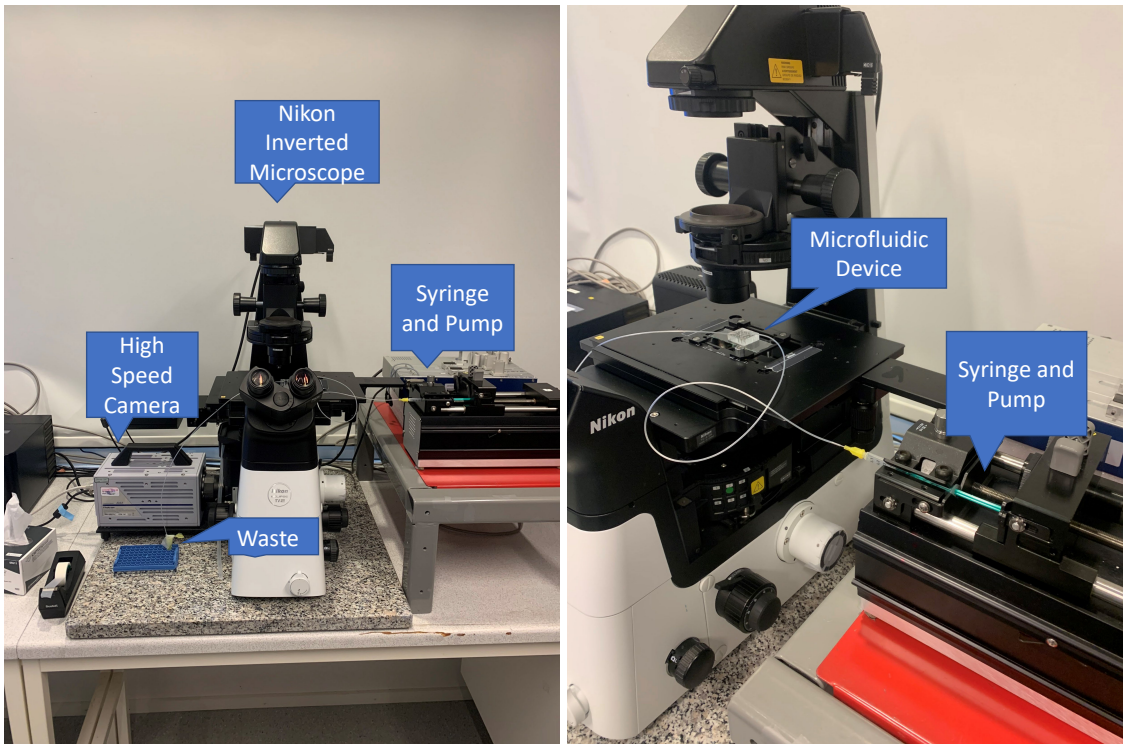

Figure 3.5: Microfluidic experimental setup. Clockwise from left to right. The high speed camera (Photron SA2) is connected to the Nikon inverted microscope at the base. As it is an inverse microscope, the light source is above the cover glass. Syringes are mounted in the pump to the right of the microscope and a waste container is placed below the microscope. The right image shows a microfluidic device mounted on the microscope, connected to a syringe loaded in the syringe pump.

The cells were stored in a centrifuge tube in a warm (37 °C) room for about an hour before starting the experiments. To start, the cells were re-suspended in solution by using a 1 mL micropipette by aspiration and dispensing of the liquid in the pipette several times, to induce turbulence in the centrifuge tube and ensure homogeneous distribution of cells.

1 mL of cell suspension was injected into a syringe (Injekt-F Luer Solo, B. Braun Medical). The syringe was gently tapped to ensure air bubbles travel to the top of the syringe and can be ejected from the solution. A 30 G needle was then connected to the syringe and to a tube (0.034" LD, 0.052" O.D, Micro Medical Tubing), and the suspension was ejected until reaching the end of the tubing. A 30 G right-angle connector was joined at the end of the tubing and entered into the inlet of the microfluidic channel. Another right-angle connector was joined to tubing and served as a waste collector.

The cover glass containing the microfluidic device was placed on a Nikon inverted microscope, with a 20X 0.45 NA objective.

The syringe was then mounted in the syringe pump (Harvard Apparatus) and firmly secured. The light, focus and field of view of the camera (Photron SA2) was adjusted. Generally, you want to record the smallest possible area, as the duration of the recording can be longer with a smaller field of view. The frame rate was set at 1000 frames per second (FPS) and the shutter speed was set at 20 000^{-1} s. The flow rate was set to 600 µL/hr. When cells were observed, a video was captured and saved in a AVI-format. The entire setup can be seen in Figure 3.5.

3.4 Video Analysis

After recording the videos, some manual processing steps are required based on the limitations of the current iteration of the Python script. Firstly, when mounting a PDMS slab on a cover glass, the channels are rarely aligned with the cover glass, meaning that the recorded videos will have microfluidic channels slightly rotated. To get accurate results from the analysis, channels should be rotated until vertical. In addition to this, simultaneity of cell passages is not supported by the current version of the code, meaning that cells cannot pass through multiple parallel channels at the same time, resulting in the need to split the video if multiple cells pass at the same time in the same recording. Both processing steps were performed

in ImageJ.

To analyse the recorded videos, the programming language Python [28] was used, utilizing the computer vision library OpenCV [29].

The first step of the script is image processing. Several image processing techniques are used, and the amount of processing might be excessive, but has proven effective for this analysis. Firstly, the image is converted to grayscale. The difference between two successive frames is calculated through the *absdiff*-function included in the OpenCV library. This essentially excludes everything which does not change between frames, i.e. pixels which are not in motion.

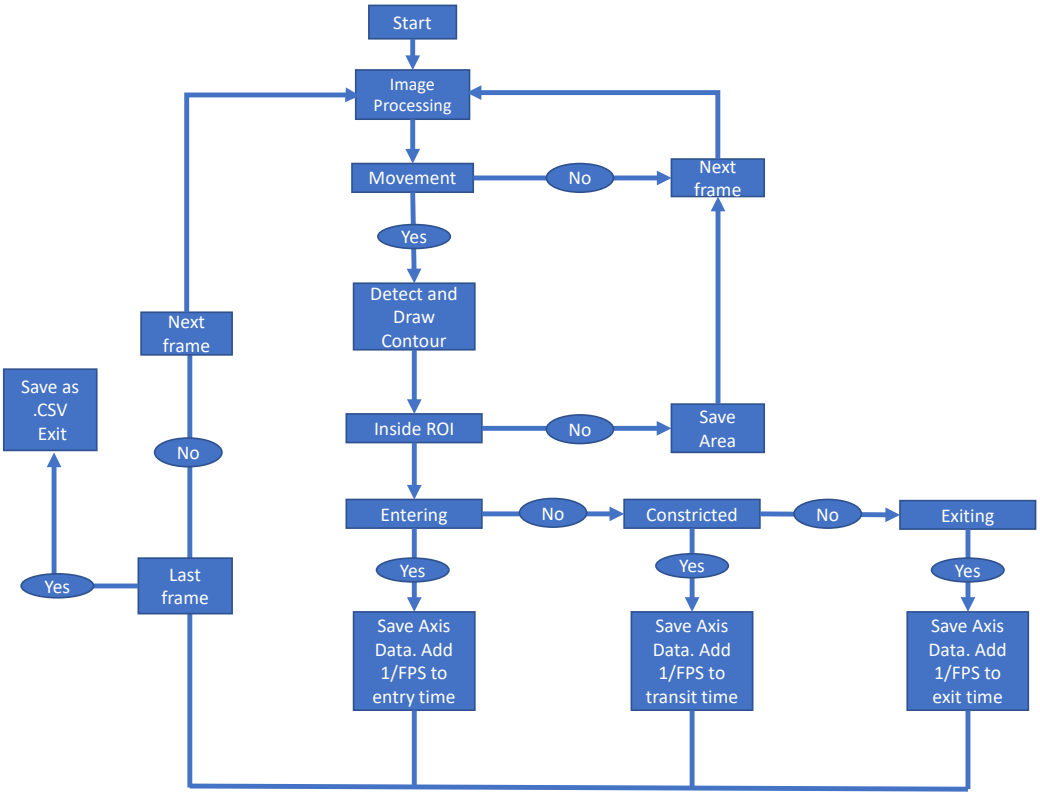

Figure 3.6: A flow chart detailing the video analysis code.

The image is then thresholded twice, firstly with a binary threshold, and secondly using Otsu's algorithm of thresholding. Finally, the image is dilated and eroded. The dilation improves the detectability of the cell, but it increases the cell area significantly. To combat this, an erosion is performed after the dilation, trying to

maintain the positive effects of the dilation while limiting the negative effects, i.e. increase of cell diameter.

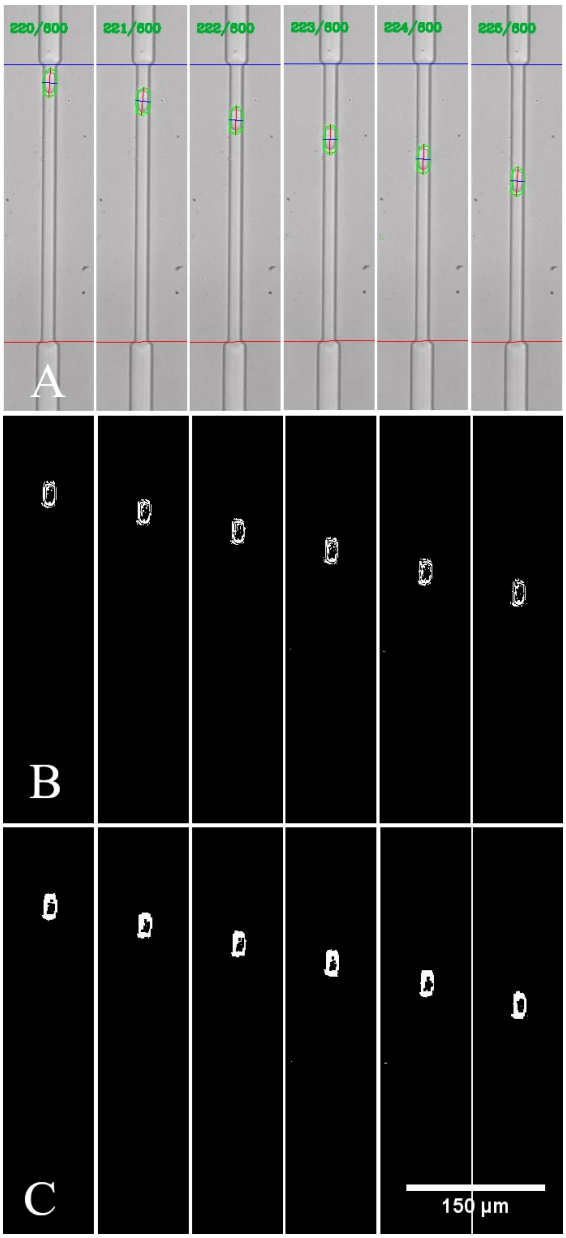

Figure 3.7: Results of various image processing techniques of the same successive frames of a video. **A**: Bright-field video of a T24 cell moving through a 10 µm by 10 µm constriction channel for six consecutive frames, with a flow rate of 600 µL/h. The blue line (top) and the red line (bottom) defines the region of interest (ROI) and is set while running the code. The green line around the cell is the drawn contour, the red line is the major axis of the approximated ellipse and the blue line is the minor axis of the approximated ellipse. **B**: The video after both thresholding methods. **C**: The video after dilation and erosion. The visibility of the cell has increased, and the size of the cell remains approximately the same as in subfigure **B**.

After various image processing techniques are carried out, movement of pixels is detected and if the area detected is above a certain threshold, a contour is drawn around the moving object. The points of this contour are used to approximate an ellipse to fit inside the contour. An ellipse is chosen because inside the constriction channel, the shape of the cell resembles that of a ellipse, apart from cell edges which are pressed into the microchannel walls, and take on a straight shape where an ellipse has curved edges.

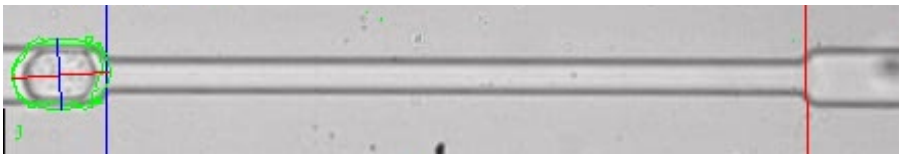

Figure 3.8: A cell considered *entering* a 10 µm by 10 µm constriction channel.

The region of interest (ROI) is determined from two lines (red and blue, Figure 3.8). When the leading edge of the cell contour touches the blue line (left, Figure 3.8) and until the trailing edge has crossed the blue line, the cells status is changed to *entering* and for each frame the cell is in this state, 1/FPS second is added to the results under entry time.

```
if (y_pos + height >= upper_line_pos and y <= upper_line_pos):
    Status = 'Entering'
    Entry_time.append(1/1000)
```

It should be noted that Y increases downwards in the image, meaning that $y + height$ is further down in the image, and is the bottom part of the cell contour, while y is the upper part of the cell contour.

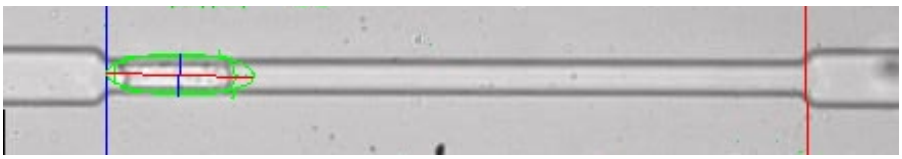

Figure 3.9: A cell considered *constricted* in a 10 µm by 10 µm constriction channel.

When the trailing edge of the cell has crossed the blue line (left, Figure 3.9) and until the leading edge of the cell touches the red line (right, Figure 3.9), the cell is considered *constricted*, and similarly to the entry time, for each frame the cell is in this state, 1/FPS second is added to the transit time. The sum of all frames in which a cell is considered constricted is defined as the *transit time*.

```
if (y > upper_line_pos and y + height < bottom_line_pos):
    Status = 'Constricted'
    Transit_time.append(1/1000)
```

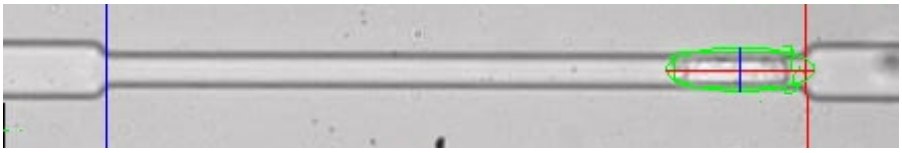

Figure 3.10: A cell considered *exiting* a 10 µm by 10 µm constriction channel.

A cell is considered *exiting* when the leading edge of the cell touches the red line (right, Figure 3.10) and until the trailing edge has crossed the red line.

```
if (y+height > bottom_line_pos and y <= bottom_line_pos):
    Status = 'Exiting'
    Exit_time.append(1/1000)
```

This process is done for every frame of the video, and the entire code can be seen in Appendix A. The code currently does not have the capability to distinguish between two cells in different or the same channel. It cannot correctly assess if a cell is the same or a different cell between two frames. This means that to get accurate results, single cell passages are necessary. In the experiments, an 8-channel constrictive region is used, and single cell passages are rare. Usually, a significant number of cells arrive at the constriction in pulses forcing a large amount of post-processing work with splitting the channels in the recording to ensure single cell passages.

The script also gathers information of a cell's velocity. This is done by adding the position of the cell to a dictionary in Python, and subtracting the previous position from the current position, and dividing by the time passed between the movement.

```
pos.append[position_current_frame]
init_pos = pos.get(i-1, [0]))
current_pos = pos.get(i, [0]))
velocity = (current_pos - init_pos / 0.001)*k
```

Where k is the scaling factor to convert pixels to micrometers.

After splitting the videos, the code can be run and the script returns a .csv-file with information about the entry times (by counting frames), the transit time and the exit time, through the constriction, as well as the minor and major axis of the approximated ellipse inside the constriction.

From the minor and major axis of the approximated ellipse inside the constrictive region, the Taylor deformation can be determined. Taylor deformation of the cell is defined as

$$TD = \frac{r_{major} - r_{minor}}{r_{major} + r_{minor}}. \tag{3.1}$$

Chapter 4

Results

The results from the experiments are presented below. Firstly, presenting cell sizes gauged by various method, followed by transit time versus cell radius and Taylor deformation, respectively. Lastly, two velocity plots are presented.

4.1 Cell Size

Initially, information regarding cell size was provided from a collaborator in Krakow, Poland. The measurements provided were significantly smaller than what was observed in this thesis work. Cell size gathered utilizing different methods are provided below in histograms (Figure 4.1-4.6), and summarized in Table 4.1.

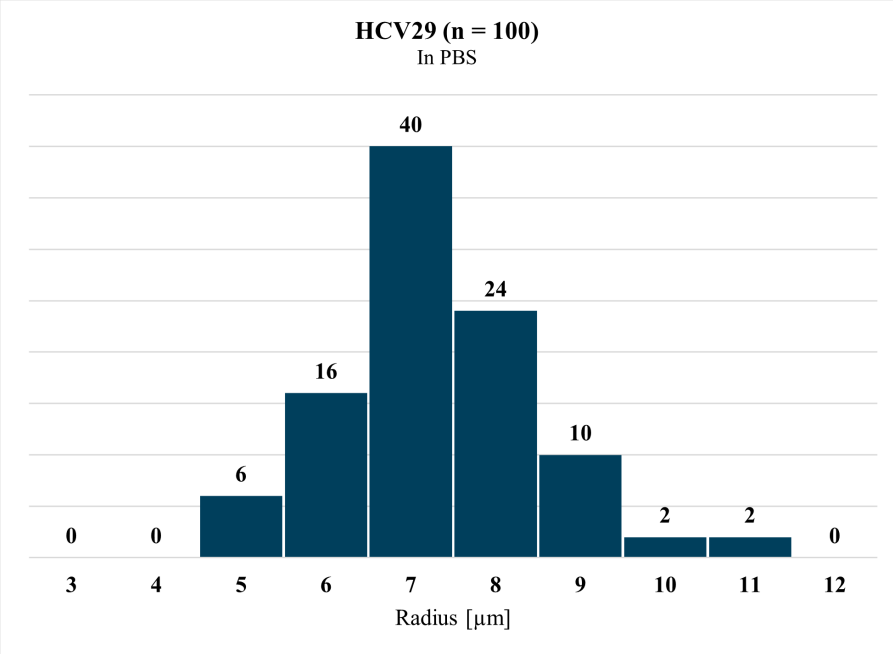

Figure 4.1: Histogram of HCV29 cell size distribution gathered by preparing cells in a suspension of PBS and imaging the cells in a Haemocytometer with Neubauer improved grid lines and using ImageJ to assess the cell size.

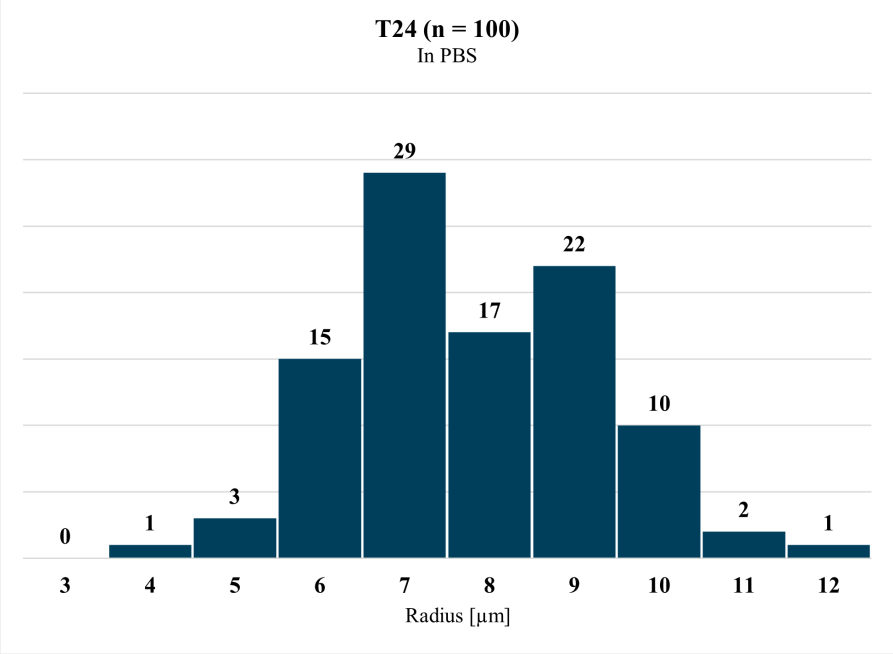

Figure 4.2: Histogram of T24 cell size distribution gathered by preparing cells in a suspension of PBS and imaging the cells in a Haemocytometer with Neubauer improved grid lines and using ImageJ to assess the cell size.

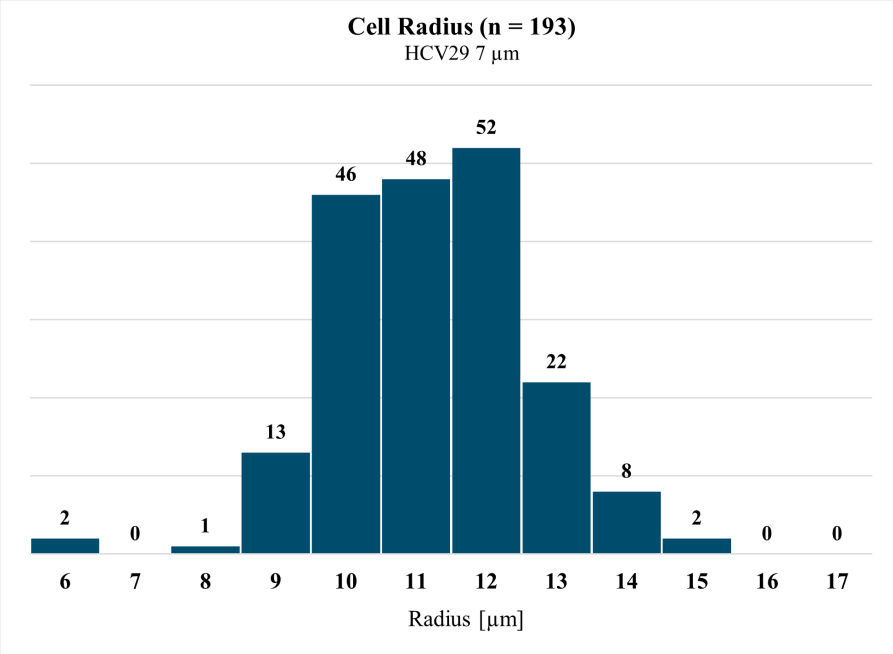

Figure 4.3: Histogram of size distribution of HCV29 cells in a microfluidic device with a 7 x 7 µm^2 constriction cross-sectional area. The data is gathered by the Python code and the area of the cell is calculated prior to the cell's entry into the constriction region.

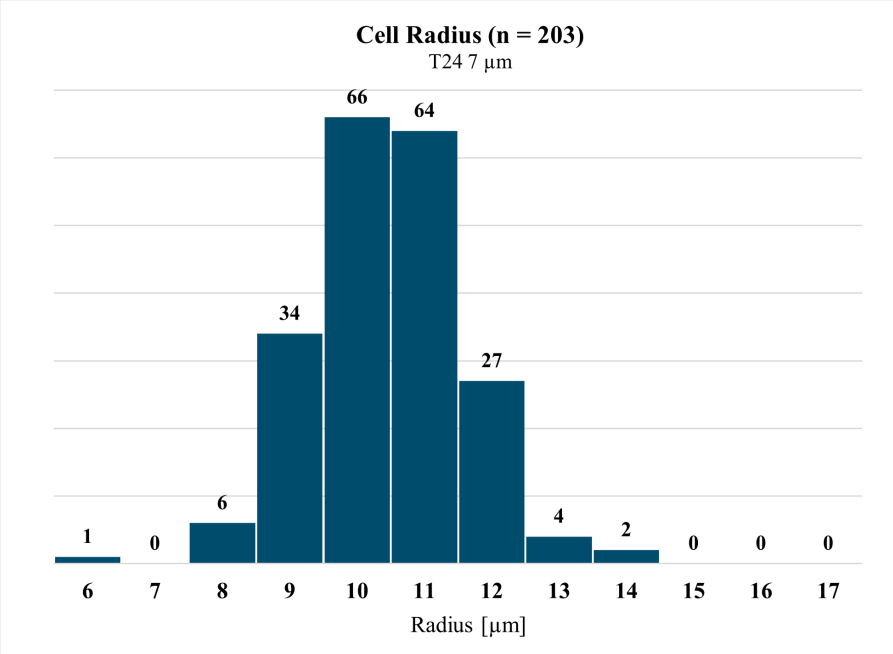

Figure 4.4: Histogram of size distribution of T24 cells in a microfludic device with a 7 x 7 µm^2 constriction cross-sectional area. The data is gathered by the Python code and the area of the cell is calculated prior to the cell's entry into the constriction region.

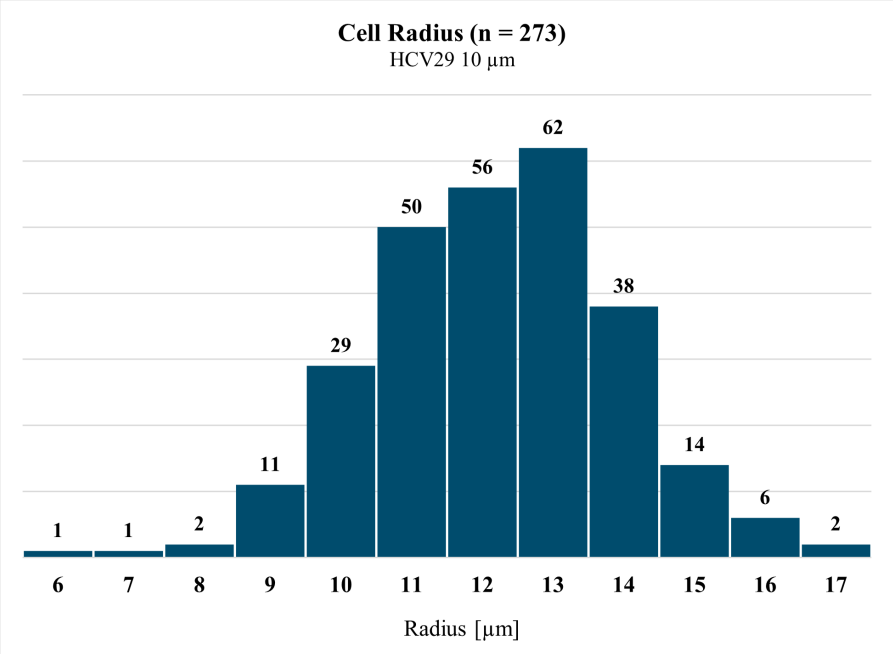

Figure 4.5: Histogram of size distribution of HCV29 cells in a microfludic device with a 10 x 10 µm^2 constriction cross-sectional area. The data is gathered by the Python code and the area of the cell is calculated prior to the cell's entry into the constriction region.

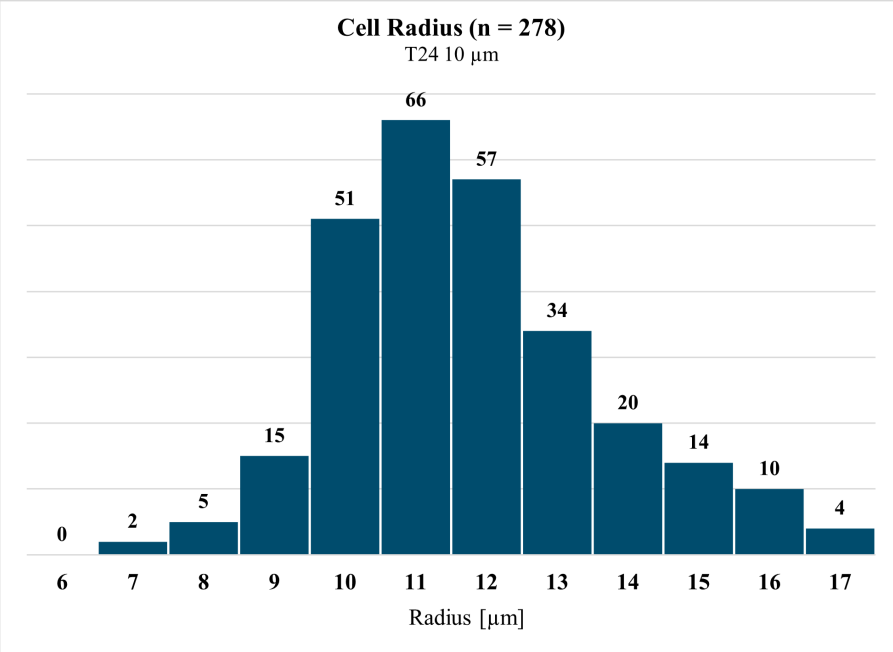

Figure 4.6: Histogram of size distribution of T24 cells in a microfludic device with a 10 x 10 µm^2 constriction cross-sectional area. The data is gathered by the Python code and the area of the cell is calculated prior to the cell's entry into the constriction region.

Table 4.1: Result of cell size measurements. Microscope measurements performed as described in Section 3.2.3. Results from cells in a microfluidic channel with 7 x 7 µm^2 cross-sectional area, and lastly, results from cells in a microfluidic channel with 10 x 10 µm^2 cross-sectional area.

Measured radius		
Method of Measurement	Size T24 [μm]	Size HCV29 [μm]
Optical Microscope	7.81 ± 1.50 (n = 100)	7.30 ± 1.14 (n = 100)
7 µm x 7 µm	10.39 ± 1.22 (n = 203)	12.23 ± 1.41 (n = 193)
10 µm x 10 µm	11.77 ± 1.88 (n = 278)	12.22 ± 1.76 (n = 273)

4.2 Transit Time

The transit time, as defined in Section 3.4 and Figure 3.9, is presented in a scatter plot versus the cell radius for each experiment and each cell type in Figure 4.7-4.10. Following this, average transit times for intervals of all radii was calculated and is presented in a histogram for both cell types and channel dimensions in Figure 4.11 and Figure 4.12. Transit time versus Taylor deformation, as defined in Section 3.4 and Equation 3.1 is presented in a scatter plot in Figures 4.13-4.16. Finally, plots for both the transit time versus cell radius and transit time versus Taylor deformation are presented in Figures 4.17-4.23.

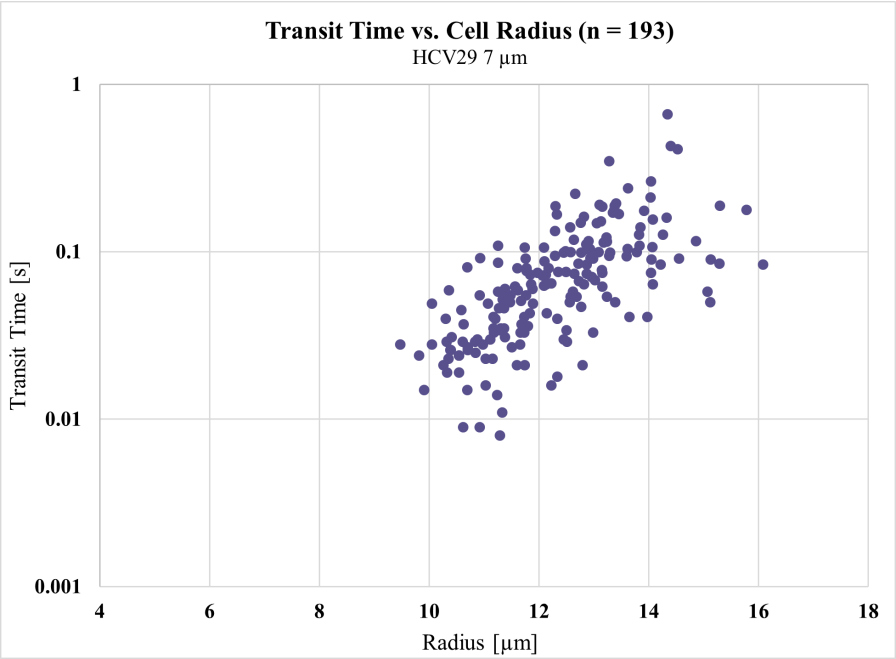

Figure 4.7: Transit time versus cell radius for HCV29 cells in a microfluidic device with a 7 x 7 µm^2 constriction cross-sectional area. The radius of the cells is gathered by the Python script prior to the cells entry into the constriction region.

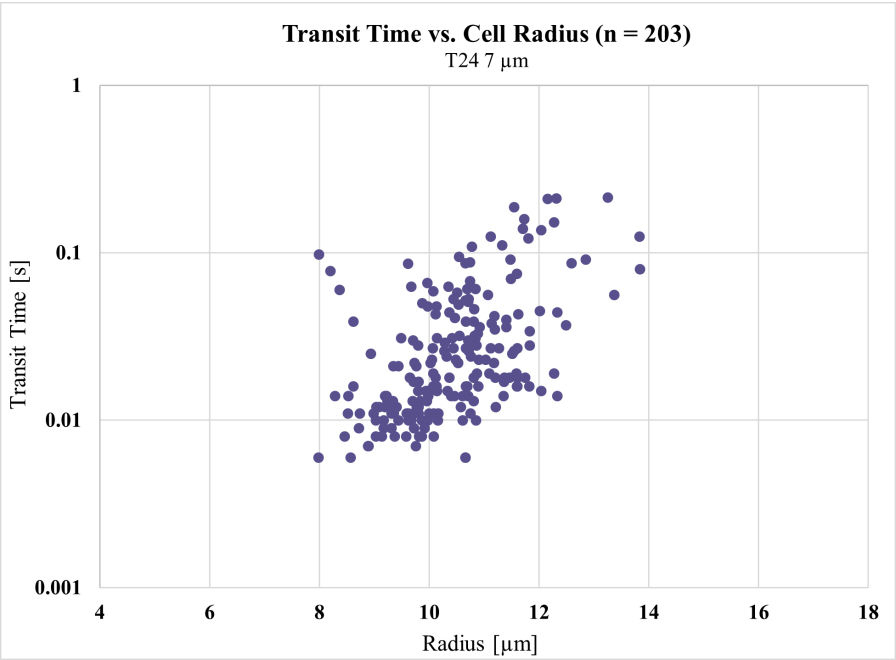

Figure 4.8: Transit time versus cell radius for T24 cells in a microfluidic device with a 7 x 7 µm^2 constriction cross-sectional area. The radius of the cells is gathered by the Python script prior to the cells entry into the constriction region.

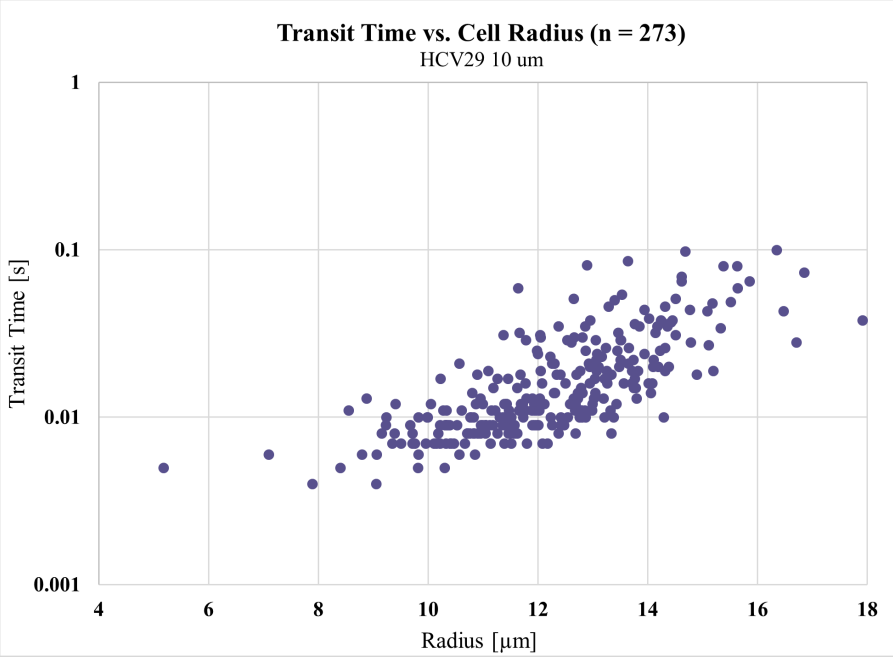

Figure 4.9: Transit time versus cell radius for HCV29 cells in a microfluidic device with a 10 x 10 µm^2 constriction cross-sectional area.The radius of the cells is gathered by the Python script prior to the cells entry into the constriction region.

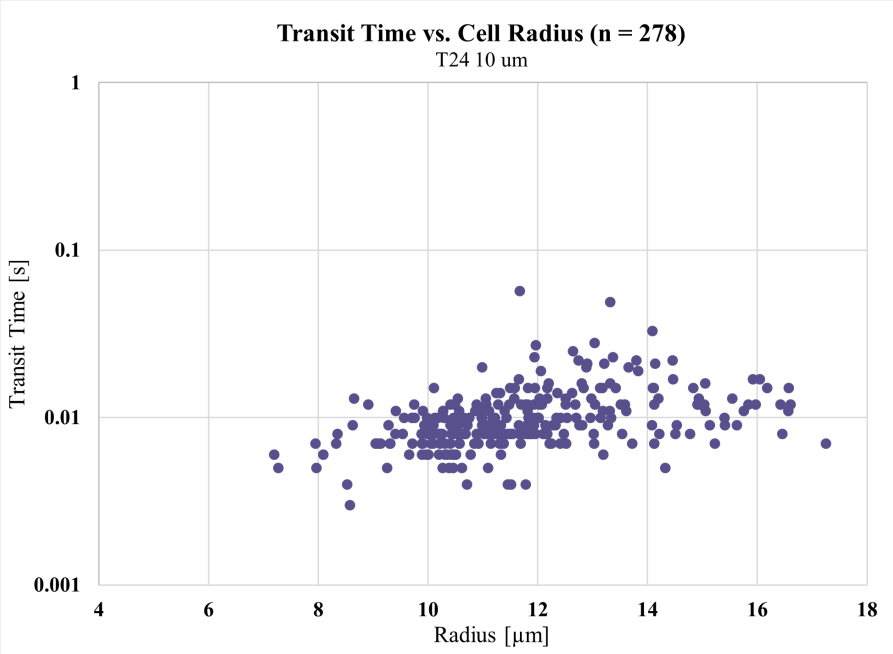

Figure 4.10: Transit time versus cell radius for T24 cells in a microfluidic device with a 10 x 10 µm^2 constriction cross-sectional area.The radius of the cells is gathered by the Python script prior to the cells entry into the constriction region.

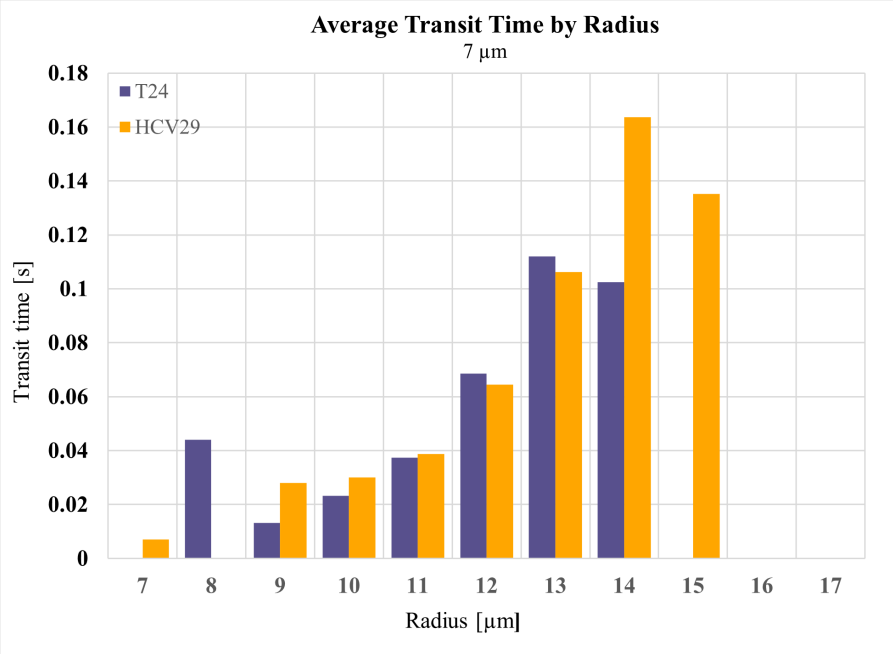

Figure 4.11: Histogram of average transit time versus cell radius for cells of the T24 and the HCV29 cell line in a microfluidic constriction device with a 7 x 7 μm^2 constriction cross-sectional area. The yellow columns are cells from the HCV29 cell line and the purple columns are cells from the T24 cell line. The radius of the cells is gathered by the Python script prior to the cells entry into the constriction region.

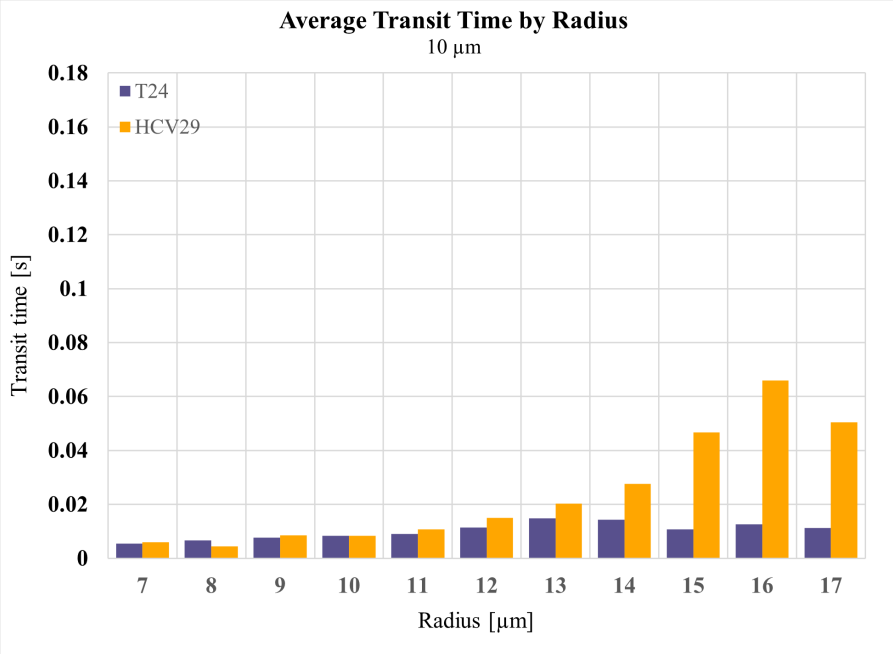

Figure 4.12: Histogram of average transit time versus cell radius for cells of the T24 and the HCV29 cell line in a microfluidic constriction device with a 10 x 10 µm^2 constriction cross-sectional area. The yellow columns are cells from the HCV29 cell line and the purple columns are cells from the T24 cell line. The radius of the cells is gathered by the Python script prior to the cells entry into the constriction region.

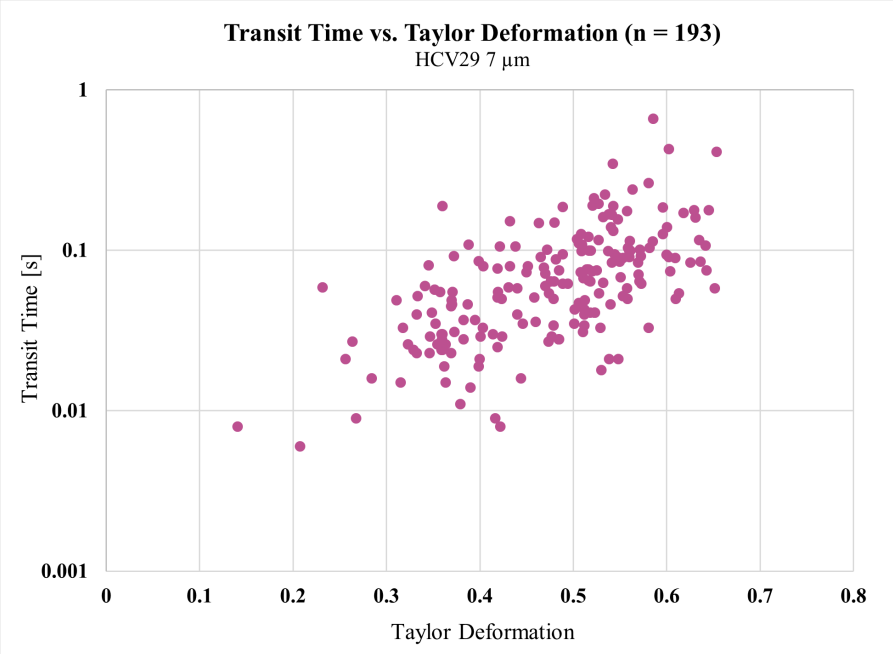

Figure 4.13: Transit time versus Taylor deformation for HCV29 cells in a microfluidic device with 7 x 7 µm^2 constriction cross-sectional area.

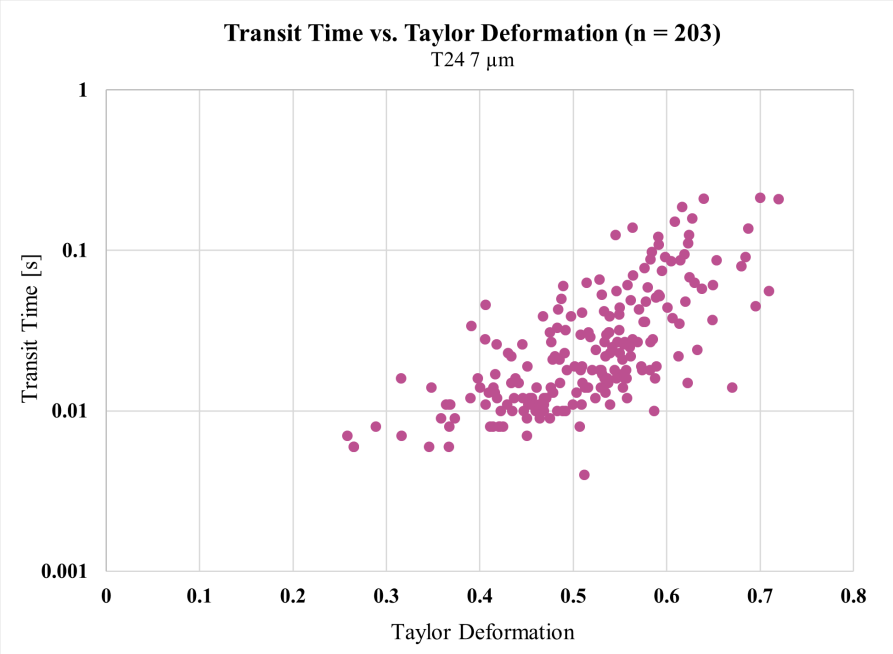

Figure 4.14: Transit time versus Taylor deformation for T24 cells in a microfluidic device with 7 x 7 µm^2 constriction cross-sectional area.

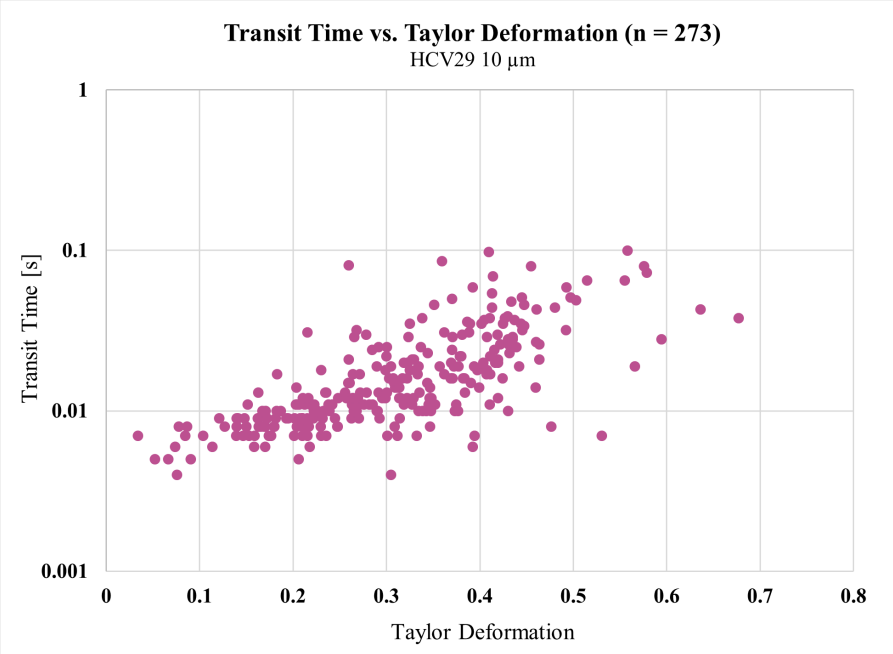

Figure 4.15: Transit time versus Taylor deformation for HCV29 cells in a microfluidic device with 10 x 10 µm^2 constriction cross-sectional area.

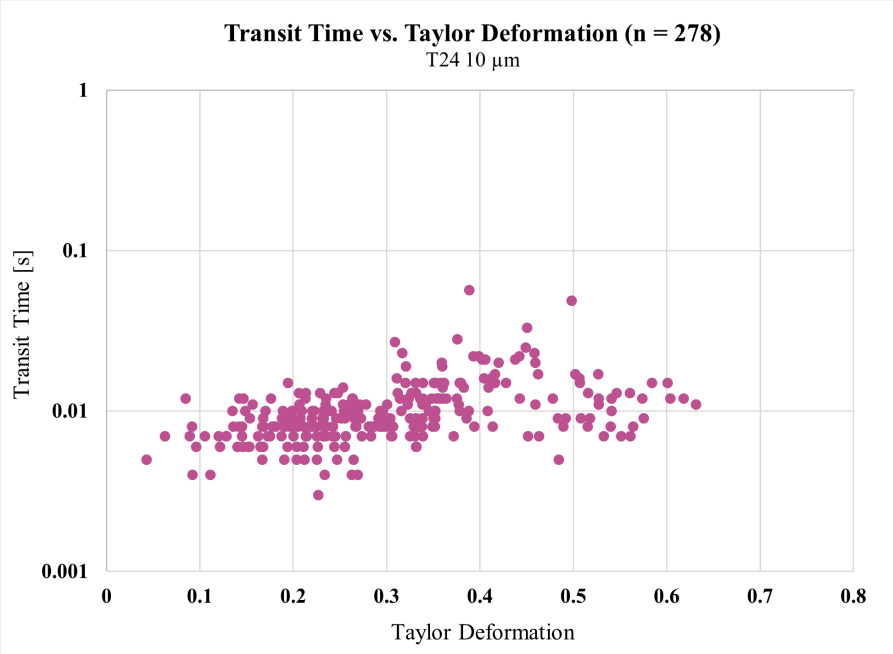

Figure 4.16: Transit time versus Taylor deformation for T24 cells in a microfluidic device with 10 x 10 μm^2 constriction cross-sectional area.

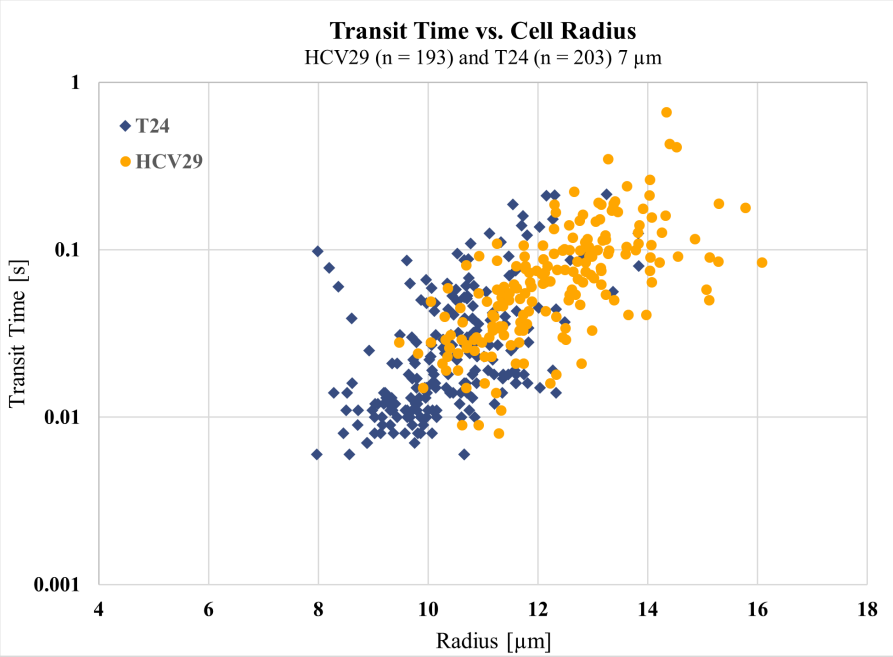

Figure 4.17: Transit time versus cell size for HCV29 (yellow) and T24 (blue) cells in a microfluidic device with 7 x 7 μm^2 constriction cross-sectional area.

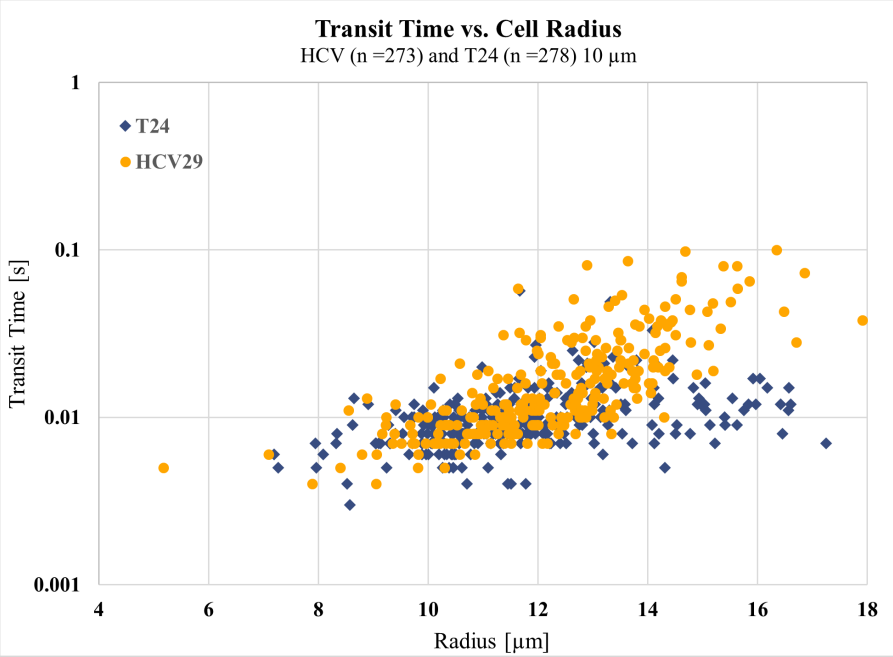

Figure 4.18: Transit time versus cell size for HCV29 (yellow) and T24 (blue) cells in a microfluidic device with 10 x 10 µm^2 constriction cross-sectional area.

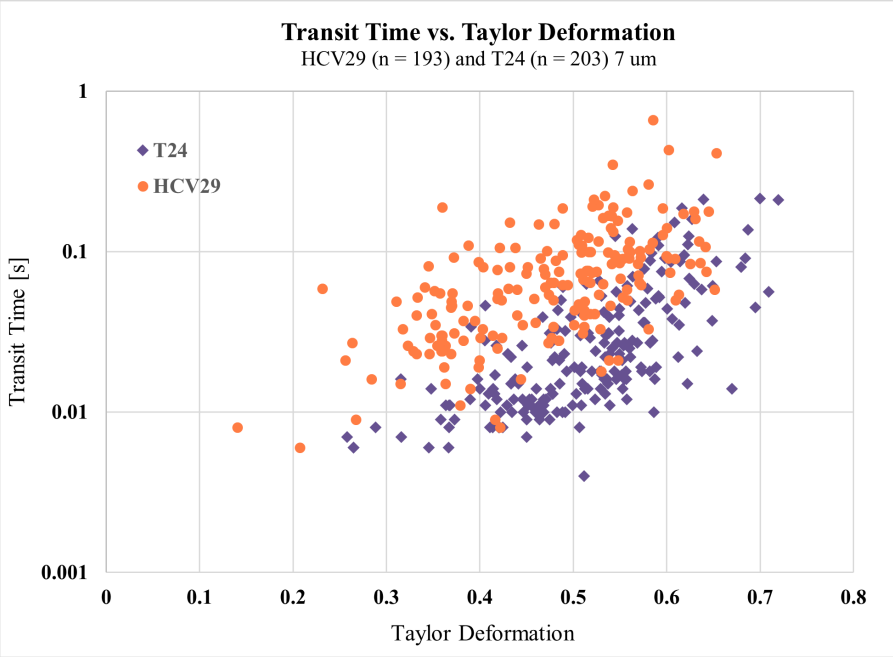

Figure 4.19: Transit time versus Taylor deformation for HCV29 (orange) and T24 (purple) cells in a microfluidic device with 7 x 7 µm^2 constriction cross-sectional area.

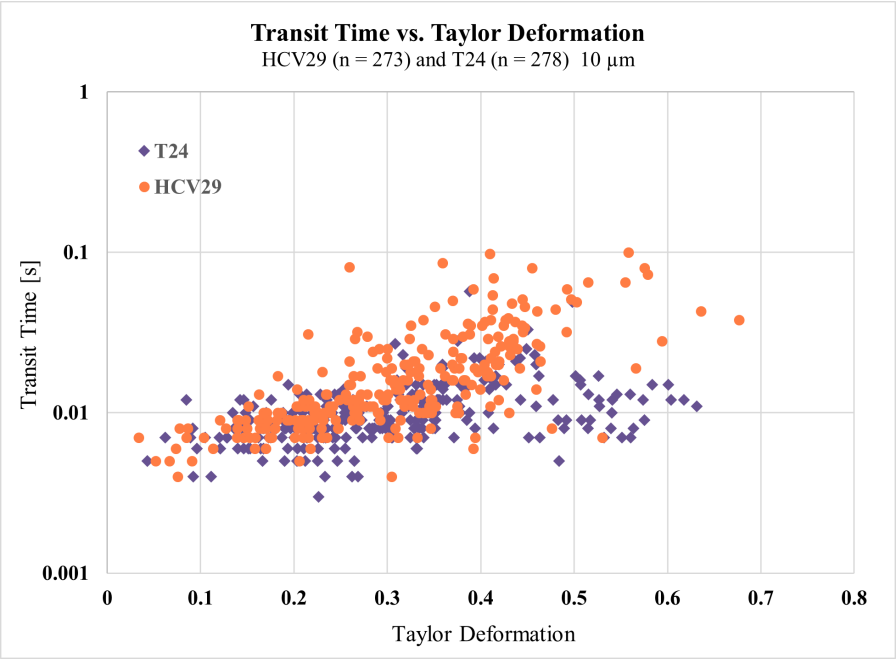

Figure 4.20: Transit time versus Taylor deformation for HCV29 (orange) and T24 (purple) cells in a microfluidic device with 10 x 10 µm^2 constriction cross-sectional area.

4.3 Velocity Profiles of Cells in Constriction Channel

Figure 4.21: Schematic illustration of the zero point and the 300 point for the velocity plots. 0 is defined as the point where the constriction starts and 300 where the constriction ends. Equivalent to µm.

The velocity profile of five cells from both T24 and HCV29 cell lines in a microfluidic channel with a 10 x 10 µm^2 cross-sectional area is presented below. The velocity profiles are based on cells of roughly the same size (r $\approx$ 12 µm). The zero-point for the plots is defined as the entry into the constriction and point 300 the exit, as illustrated in Figure 4.21. Negative position-values denote a position prior to entry and position-values above 300 denote positions after exit of the constriction

region.

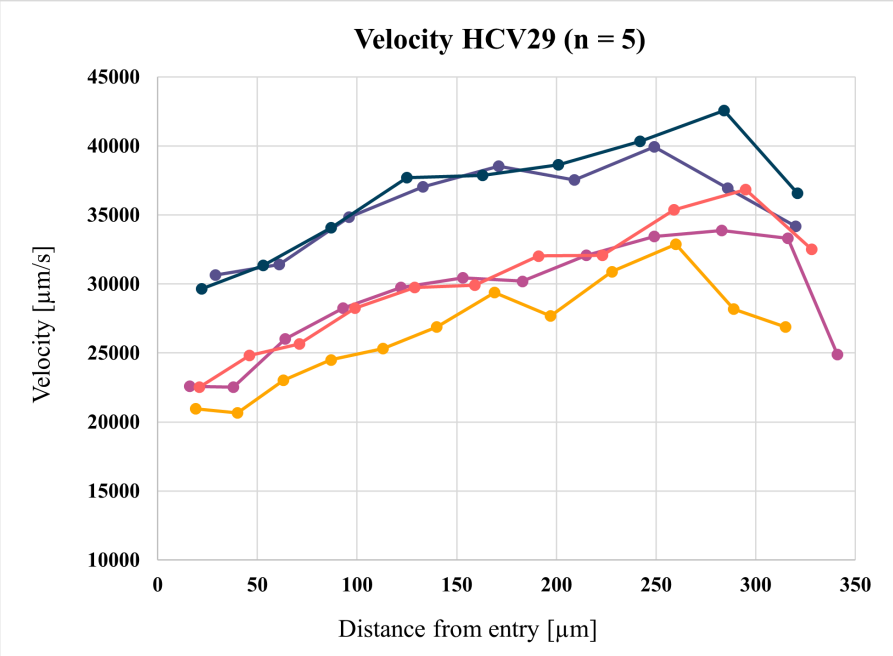

Figure 4.22: Velocity profiles of five HCV29 cells in a microfluidic constriction device with 10 x 10 µm^2 constriction cross-sectional area at a flow rate of 600 µL/h.

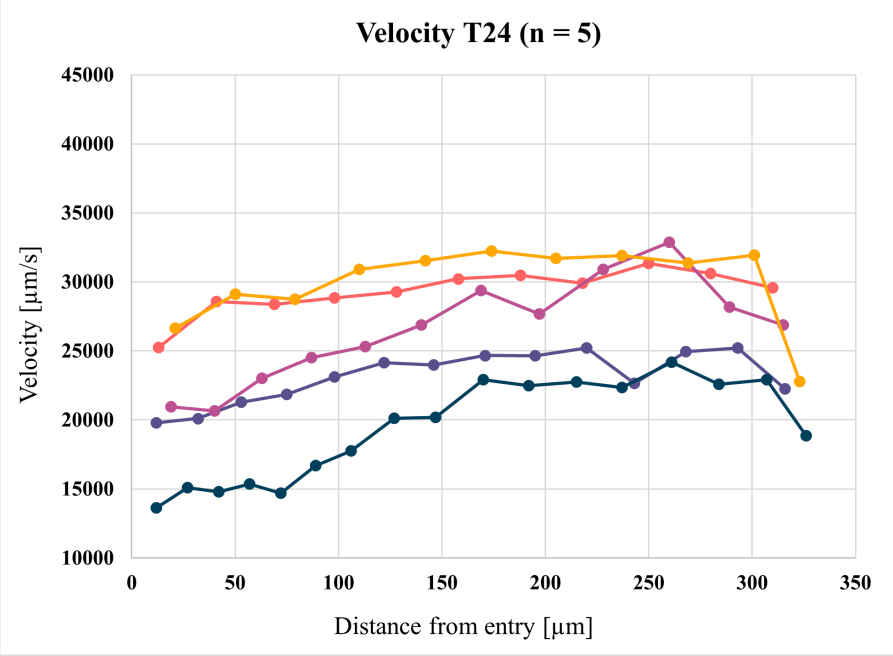

Figure 4.23: Velocity profiles of five T24 cells in a microfluidic constriction device with 10 x 10 µm^2 constriction cross-sectional area at a flow rate of 600 µL/h.

Chapter 5

Discussion

5.1 Microfluidic Device Fabrication

Fabrication of the microfluidic devices used in this thesis work has been streamlined and based on existing protocols. Nevertheless, some optimizations of the process should be explored.

Currently, exposure of the silicon wafer has been performed with the same dose (320 mJ/cm^2) for both the 10 µm and the 7 µm coats of photoresist. The dose may be somewhat excessive for both thicknesses, and especially the 7 µm coat. A dose-response and development test could be conducted to ascertain the optimal doses and development times going forward.

Development of the photoresist has also given rise to challenges, with development times ranging vastly, from about 6 minutes to about 11 minutes. For reasons unknown, no set time has been found to work for all coats of the same height consistently, and successful development is dependent on inspecting the wafer under a yellow light microscope to ensure proper development. If the resist is not satisfactory developed, a second development is initialized. The efficacy of multiple developments is unknown, but experimentally, the development can be completed after secondary developments, performed in increments of 1 minute, followed by

inspection.

The soft lithography workflow has, in the same manner as the photolithography process, been streamlined. Factors which could be considered for further optimization are the baking time, the ratio of curing agent to PDMS pre-polymer, the method and forcefulness of bonding the PDMS to glass, the post-bonding bake and the storage conditions.

Regarding the concentration of the PDMS pre-polymer and the curing agent, there are conflicting findings. Sharfeddin et al. conducted studies where Young's modulus of PDMS was measured for PDMS pre-polymer cross linker ratios spanning from 50:1 to 10:1 and found no change in macro scale difference in elastic modulus from 5:1 and 2.5:1 ratios [30]. On the other hand, Mfoumou et al. which studied cross-linker concentrations from 3.3 to 33.3 wt% found an increase in Young's modulus, which plateaued at 20 wt%, corresponding to 5:1 pre-polymer to cross linker ratio [31]. It is therefore challenging to conclude whether or not an increase in cross linker concentration would increase Young's modulus of the cured PDMS. As this thesis work involves deformation and compliance, all though with soft objects, rigid walls of the microfludic channel is important. If, or how, this affects the data presented is unknown. The common practice for mixing PDMS is a ratio of $10:1$ PDMS and cross linker and researchers performing soft lithography are strongly encouraged to follow this ratio by the engineers at the local lab. Also, both Sharfeddin and Mfoumou found a Young's modulus of the $10:1$ PDMS to cross-linker ratio to be just below 2 MPa which is significantly higher than the Young's modulus of the cells which lie in the 1-10 kPa range Lekka et al. reported in 1999. [30, 31, 9].

In addition, the storage conditions of PDMS have been shown to affect the Young's modulus of the cured PDMS, where Agoglu et al. reported that a humidity between 10% and 85% resulted in linearly decreasing Young's modulus [32]. The baking performed after the bonding step can therefore be prolonged indefinitely, until the device is needed, as a method to reduce the amount of humidity the microfluidic

device is exposed to.

When plasma activation has been performed on the PDMS and the glass, the PDMS is mounted on the glass slide. To achieve adequate bonding, gentle pressure is applied to the PDMS. Excessive force during this stage can lead to the channel bonding to the glass slide, causing bonding issues and leakages in the final channel. The frequency of this occurring increases with increasing aspect ratio between channel width/height. The roof of a channel bonding to the glass is a more common problem for wider channels with lower heights.

5.2 Microfluidic Experiments

Initially, given information from collaborators in Poland regarding size of the cells, a device with a 7 x 7 μm^2 constriction cross-sectional area was chosen for the constriction experiments. When running the experiments, this channel size was deemed too small to efficiently run experiments with both cell lines, as clogging was a major issue and gathering results became challenging when multiple channels were clogged within minutes. One image of a clogged device can be seen in Figure 5.1, where no cells were moving at the time of imaging, meaning that most channels were clogged. The placement of arrested cells varied, where they sometimes were observed arrested at the bifurcation prior to the constriction, and in other cases in the start or the middle of the constriction itself.

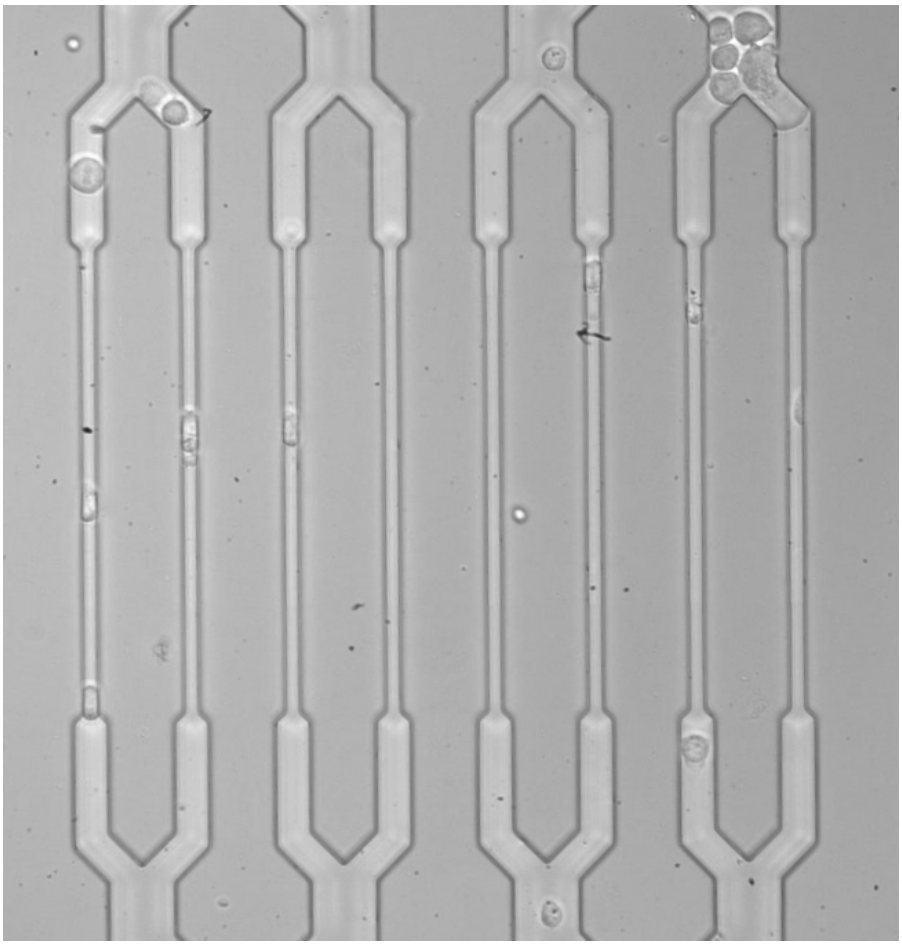

Figure 5.1: Microscope image taken during experiment with a 7 x 7 µm^2 constriction channel with T24 cells. As can be seen, substantial clogging has occurred in the constriction domain as well as in the previous bifurcation, barely allowing any cells to pass. No cells were moving at the time of imaging, i.e., all cells seen in the image were arrested in place.

When running experiments, clogging was observed for both channel sizes (10 µm and 7 µm), but the frequency of clogged channels was higher for the lower dimensions.

The concentrations of cells in PBS when running the experiments may also have been excessive. The experiments in this thesis were performed with a concentration of 400 000 - 800 000 cells/mL PBS. Even at the lowest concentrations (400 000 cells / mL), a substantial number of cells were observed to intermittently reach the constriction region in notable pulses. A lower concentration and larger dimensions may reduce the frequency of clogging, and could be explored if the problem persists.

In addition, all experiments in this thesis were done with a flow rate of 600 µL/h. As the cells pass very quickly for this flow rate, a reduction in flow rate may reduce the clogging and still provide a high enough throughput.

The functionalization with Bovine Serum Albumin (BSA) is performed to limit non-specific adherence between cell surface and PDMS channel walls. Initially, the functionalization was conducted with unfiltered BSA which led to aggregates of BSA clogging the constriction region of the channels. Filtration four times, with 1.2 µm, 0.8 µm, and 2 x 0.2 µm was found to reduce the clogging effect and the detriment of BSA to the flow of cells through the channels. However, the efficacy of the BSA functionalization is unknown for these experiments. Trial experiments were done without BSA and no difference in cell behavior was observed by visual inspection.

For this work, cells have been suspended in PBS for experiments, due to cell medium having a tendency to generate air bubbles when agitated. After being suspended in PBS, the suspension is placed in a warm room for 1 hr to allow the suspension to settle. Information provided by lab engineers suggest that the most effective storage method for cells in PBS is in a fridge or on ice. The reasoning for this is that when cell medium is removed from the cells and they are suspended in nutrient-free PBS, the cells begin to starve. This starving is exacerbated in warmer temperatures, and a reduction in temperature would essentially lower the metabolism of the cells, allowing them to stay viable for longer. A suggestion would be to split the suspension in several 2-3 mL vials which are stored in the fridge and perform experimentation on one vial at the time to increase the longevity of the experiments, if needed. As PBS increases viscosity significantly, as well as the fluidity of the cell membrane being affected by lowering the temperature, the cells should gently be allowed to reach room temperature prior to experimentation.

5.3 Cell Culture Work

Confluence, denoting a measurement of cell density on the surface where an adherent cell culture grows, e.g., the bottom of a culture flask or culture dish, is an important parameter to control for experimental repeatability. The way confluence has been measured for the experimental work of this thesis is by qualitative, visual measurement of the cell flask through an optical microscope. This gives rise to variations from researcher to researcher and is not particularly reproducible. In addition to this, different cell lines should be split at different levels of confluence. Cell behavior and kinetics may change if the cells grow too closely. Topman et al. report that myoblasts or pre-adipocytes undergo spontaneous differentiation into myotubes and lipid-droplet containing adipocytes at high confluency. Similarly, cells can undergo morphological changes at higher confluency [33]. The cells used in this thesis experimental work have been split and used at different levels of confluency, with the goal of splitting and using at ≥ 80 % confluency. There has not been used any quantifiable methods to determine level of confluency and the repeatability sufferers thereafter.

Secondly, the age of the culture may factor into some effects of the observed results. The last experiments were performed with cells from the 18th passage, meaning the cells had been split 18 times prior to experimentation. If and how this affects the results is unknown.

5.4 Analysis

Several challenges still remain with the analysis of the recorded videos. Firstly, the recording is limited to a couple of seconds depending on the resolution and FPS setting of the camera. With the settings used for this work, a video length of 3.6 s was possible for each recording. Another challenge with the recording is the save time, which is currently over 2 minutes per video. It is not possible to record while saving a video, meaning most of the cells are passing by while saving a video.

For the script to detect cells, several processing techniques are currently necessary. Firstly, the image is dilated. Dilation significantly increases the area of the dilated object, and an erosion is performed to reduce the area of the dilated cell. The erosion helps somewhat, but the area is still overestimated, as can be seen in Figure 5.2. Secondly, an ellipse is not the ideal shape of the cell to approximate the cell shape to. Generally, the cells are round before entering the constriction, and pill or bullet shaped inside the constriction. An ellipse gives two parameters, the minor and major axis, which are used to calculate the Taylor deformation of the cell. A more fitting approximation may help the accuracy of the results and should be explored.

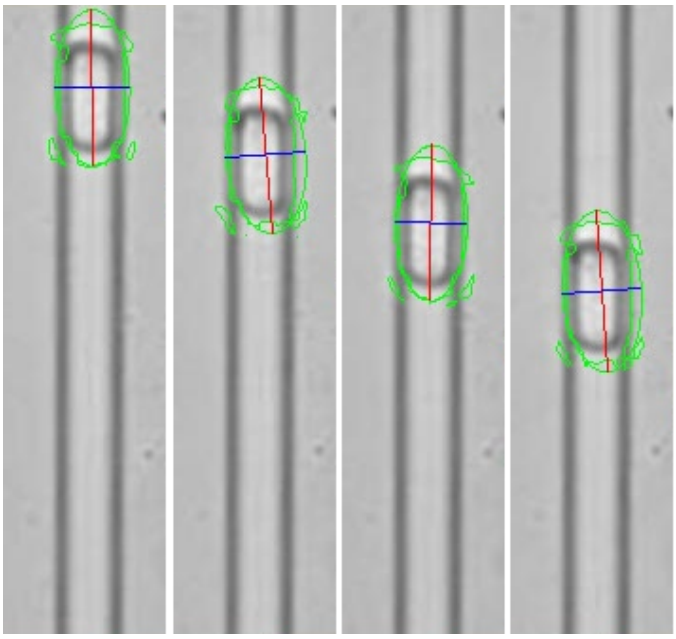

Figure 5.2: Consecutive frames of a cell passing through a constriction channel with dimensions of 10 µm x 10 µm. Contours of the cell drawn in green, as well as minor (blue) and major (red) axis. As can be seen, the contour of the cell is significantly larger than than the cell, particularly in the axis of movement.

Running of the analysis after recording the videos is still quite demanding and time consuming, and requires a significant amount of manual editing. Firstly, due to the script not being able to register two cells passing at the same time, in the same or parallel channels, as different, videos should only contain single cell passages

at one time. This is due to the script performing the same image processing for each frame of each video and has no way to identify if the cell in the current frame is the same as the cell in the previous frame. There exist several ways to address this, one might be able to identify the cell based on trajectories, if the cell is moving in a straight line in a specific section of the frame, between two frames it is likely the same cell. This would address the issue with parallel passages, but multiple passages in the same channel would still remain an issue. There are also methods for image recognition used with cars, for instance, where a programming language can be utilized to identify different cars from a video. This works mainly by recognizing shape and color, and would be challenging to implement for cells, as cells are largely homogeneous, both in shape and color, meaning that distinguishing cells based on these characteristics would be demanding.

The microfluidic device has 8 parallel constriction channels, and parallel passages often occur in videos, resulting in a substantial amount of processing work. Secondly, the script returns the data gathered in a .csv-file, requiring the user to manually identify a cell passage by checking the sequential status of a cell (that is, *entering*, followed by *constricted*, followed by *exiting* without interruption). Nevertheless, the code is a foundation for further development, and OpenCV has many interesting compatabilities, for instance with using live streams as the video source, ideally making a real-time high-throughput analysis possible in the future.

Another challenge with the setup used today is the lack of a digital focus, resulting in videos sometimes having different focus, and the edges of the cells having varying amounts of contrast. Adjusting the focus while running experiments has been challenging, as cells pass too quickly to adjust focus while cells are in movement inside the channels. A digital focus would help, as you could use exactly the same focus for each experiment, and streamlining the analysis more. For different focuses and light settings, changes in thresholding are sometimes required, making the analysis more demanding.

5.5 Transit Time

In 1999, Lekka et al. published a study where scanning force microscopy was used to determine elastic properties of various living cells. They found a one order of magnitude difference in Young's modulus between cancerous cells and non-malignant counterparts. More specifically, a Young's modulus of 10.0 kPa was determined for HCV29 (non-malignant) and 1.0 kPa for T24 (malignant) [9]. In this study, the difference in deformability is attributed to the pericellular matrix, cell membrane and cytoskeleton. The same group performed another study in 2012, using atomic force microscopy (AFM) to show a lower Young's modulus for single cells of various cancers, such as bladder, melanoma, prostate, breast and colon [10].

Cross et al. reported using nanomechanical AFM that metastatic cancer cells and benign mesothelial cells, where metastatic tumor cells are more than 80% softer than their benign counterpart. Further, the research states that morphology alone is unlikely to explain the significant difference in elastic moduli for the two cell types. In addition to softness, non-specific cell adhesion was analyzed and tumor cells were found to be approximately 33% less adhesive compared to normal cells [34].

The three studies presented above utilized single-cell analysis methods, where one cell is measured at a time. A high-throughput method to analyze a larger number of cells in a shorter amount of time is desired, and microfluidics provides a solution for this. The benefits of using a microfluidic approach, in addition to high throughput, is a more life-like way to measure cell deformation in microfluidic channels which can somewhat mimic blood vessels. Some challenges arise when using a microfluidic platform, being that there is no simple way to extract the elasticity of the cell based on observable characteristics in a microfluidic channel [17]. The data gathered in a microfluidic deformation channel can for instance be used in finite element analysis (FEA) to create a model for elasticity of the cells.

In a review article from 2020, Urbanska et al. compares three different microfludic

approaches for cell deformability measurements, shear flow deformation cytometry (sDC), extensional flow deformability cytometry (xDC) and constriction-based deformability cytometry (cDC). The work in this thesis has been done with a constriction-based deformability cytometry, and for this Urbanska et al. define the deformability parameter D as the inverse of the cell transit time [23].

From Figure 4.11 and Figure 4.12 a difference in trends for cancerous (T24) and non-malignant (HCV29) cells can be observed, especially for the channel with 10 x 10 µm^2 constriction cross-sectional area. For the larger cells of the non-malignant cell line, the average transit time is significantly higher than that of the malignant cell line, which suggests that the cancerous cell line might be more deformable than the non-malignant one. One can also observe that the distribution of data points in Figure 4.10 is quite flat, which suggests that the transit time for T24 cells is less size-dependent than for HCV29. All though not as significant as Lekka's results from 1999, with a difference in one order of magnitude between T24 and HCV29, the two populations can be separated visually in Figure 4.17, Figure 4.19, and to a lesser degree in Figure 4.23.

5.6 Entry Time

Entry times may be more relevant for assessing the viscous deformation of a cell, i.e., the time it takes for the cell to fully comply to the reduction in channel size and enter the constriction. The entry time of cells vary greatly, and for reasons not fully understood. For instance, both Figure 5.3 and Figure 5.4 are from the same cell line (HCV29), both cells have similar dimensions, the cell in Figure 5.4 being somewhat larger, and both cells are entering a channel with a 10 x 10 µm^2 cross-sectional area. Interestingly, the time it takes for the cells to enter is vastly different. The cell in Figure 5.3 is considered *entered* after just six frames, corresponding to 6 ms. The cell in Figure 5.4 spends over 10 fold more time in a state of *entering*, spending 70 frames and 70 ms in this state.

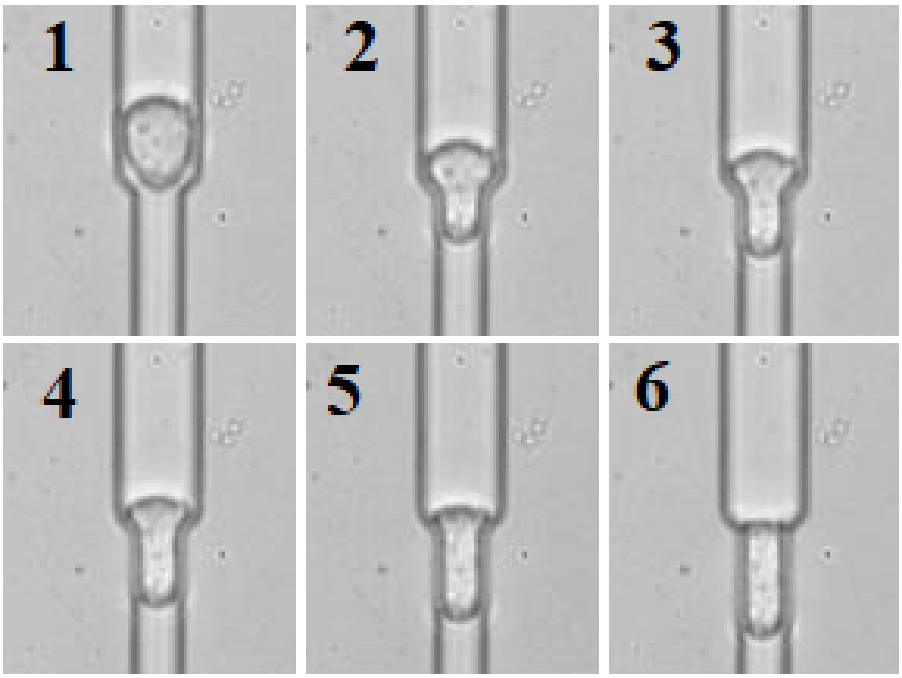

Figure 5.3: Entry of a HCV29 cell into a microfluidic channel with 10 x 10 µm^2 constriction cross-sectional area. Considered somewhat fast, as it uses 6 frames to enter, equivalent to 6 ms. The number in the figure marks the frame of the image.

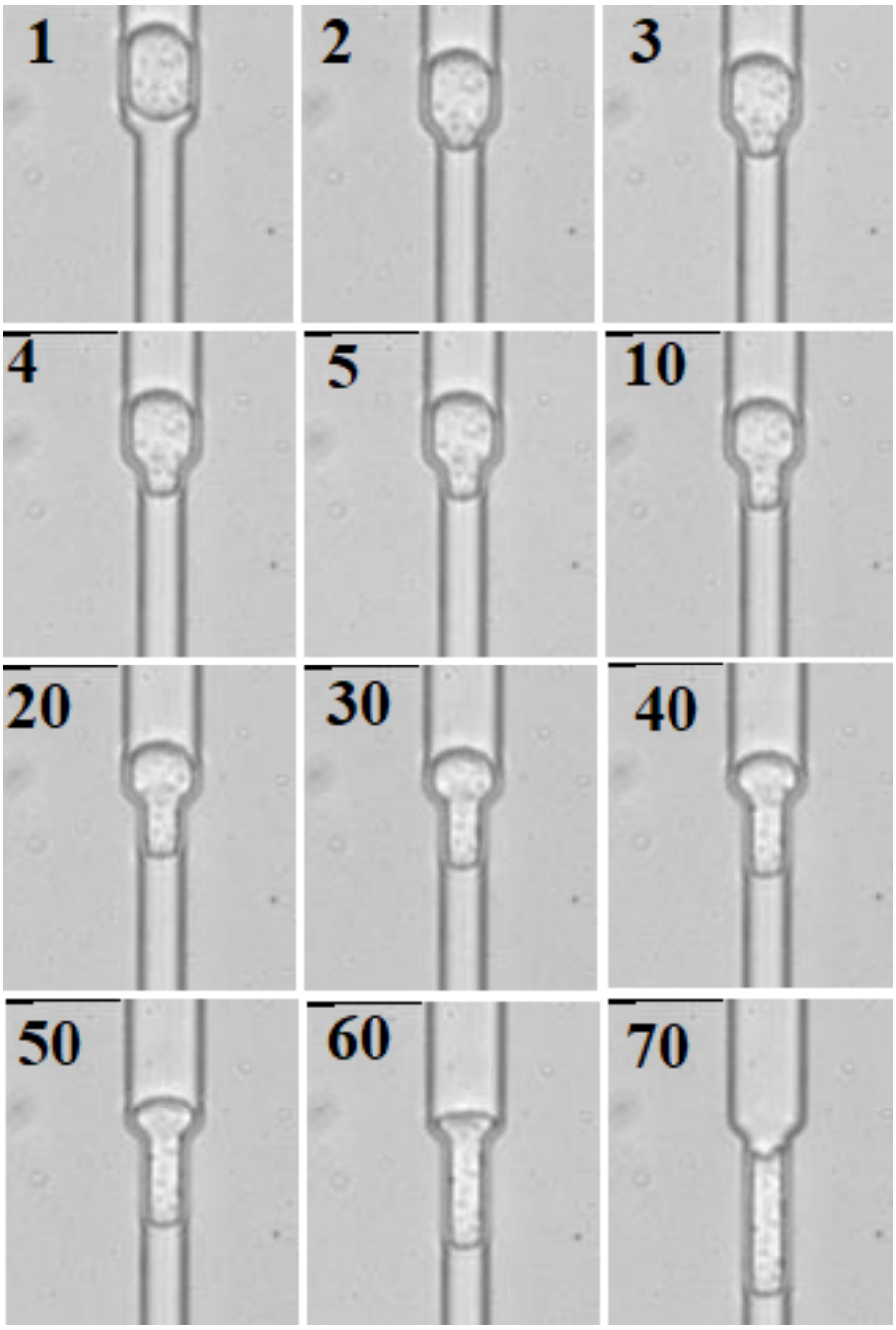

Figure 5.4: Entry of a HCV29 cell into a microfluidic channel with 10 x 10 µm^2 constriction cross-sectional area. Considered a slow entry, as it uses about 70 frames to deform enough to fit into the channel, which corresponds to 70 ms. The number denotes the current frame of the image. Note that the frame starts skipping ten frames ahead after frame 5 for brevity.

5.7 Elastic, Viscous, Viscoelastic or Plastic

Depending on the time scales and the mechanical forces applied, cells exhibit both solid-like elasticity and fluid-like viscosity, which is called viscoelasticity [22]. This is further supported by Gensbittel et al., which elaborates and states that an elastic cell which is capable of instantaneously and reversibly deforming with an object has significantly different mechanical properties from a cell progressively making its way across a constrictive blood vessel for a longer time period [17] (Figure 5.5). Based on this, the cells observed in a microfluidic constriction device are likely to exhibit both viscous and elastic properties.

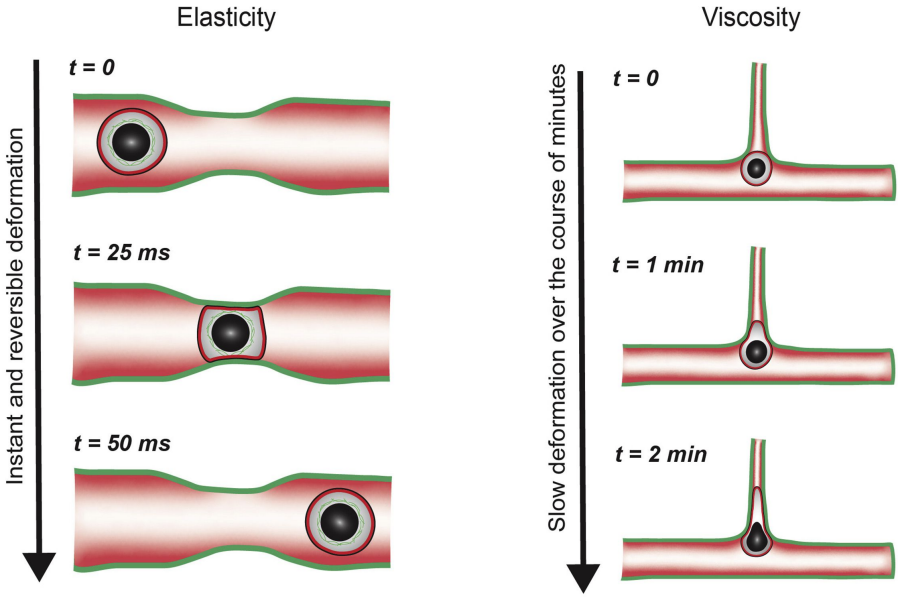

Figure 5.5: Elasticity and viscosity of cells. Adapted with permission from [17], which states that elasticity works for very short time scales, while viscosity occurs when a cell is mechanically challenged for a prolonged period of time.

A cell in the entry part of the constriction channel, is likely to be dominated by viscous properties (viscosity part of Figure 5.5) and the transit after entering would be modeled by the elasticity part of Figure 5.5. Nevertheless, during the cell experiments, some cells retained their deformed shape after exiting the deformation channel. The extent of deformation varied significantly, where some cells did not retain the deformed shape at all and immediately returned to their initial shape, while others retained their deformed shape for a longer time. How long is difficult

to gauge, as the field of view when running experiments is limited to about 50 µm below the exit of constriction channel. Two types of deformation can be seen in Figure 5.6, where deformed HCV29 cells are shown in both a 7 µm x 7 µm channel and a 10 µm x 10 µm channel.

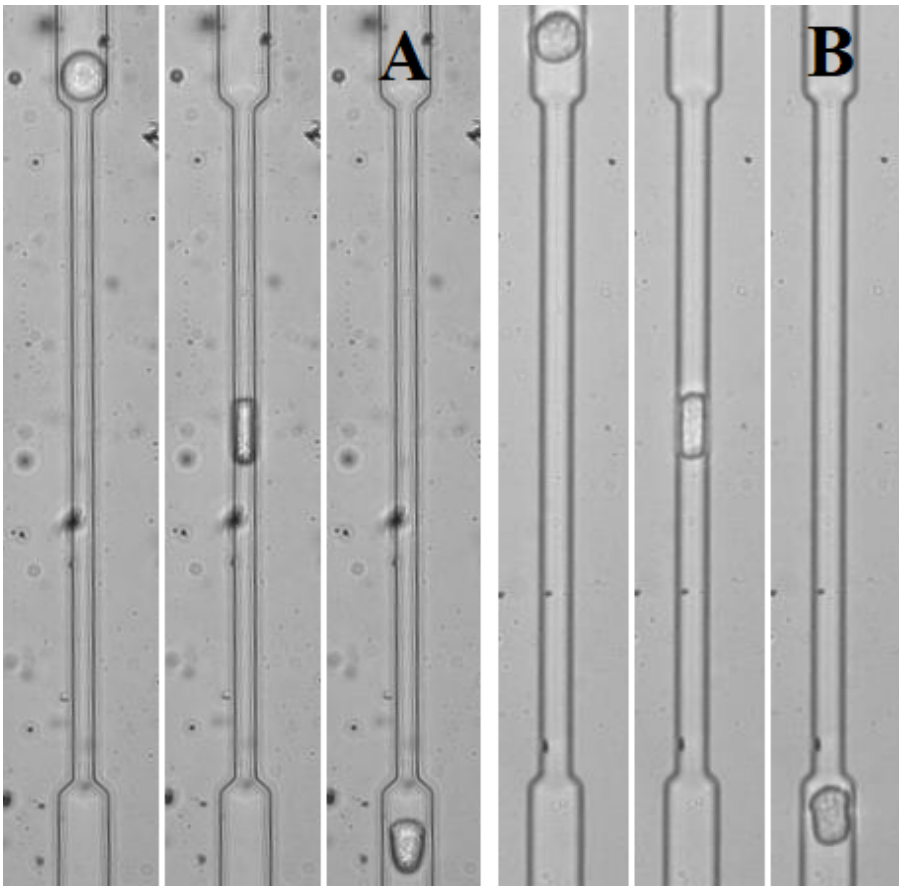

Figure 5.6: **A**: A HCV29 cell entering, being constricted and exiting a microfluidic channel with 7 x 7 μm^2 constriction cross-sectional area. The shape is somewhat retained after exit in a sort of pear-shape. **B**: A HCV29 cell entering, being constricted and exiting a microfluidic channel with 10 µm x 10 μm^2 constriction cross-sectional area.

The extent of deformation seems somewhat size dependent, where smaller cells retain their deformed shape less frequently than their larger counterparts. The shape of the deformed cells after exiting the constriction channel has also been observed to vary, where some cells retain a bullet-shape, similar to what can be seen in Figure 5.6, **B**. Other cells may have a pear-shape, where the end of the cell is larger than the front, which can be seen in Figure 5.6, **A**. The reasons for

this variation in shape is unknown, but could perhaps be attributed to which part of the channel the plastic deformation occurs. If the deformation occurred in the entry part of the channel, a cell might exhibit deformation imaged in Figure 5.6,**A**, while if the plastic deformation occurred more in the middle of the deformation channel, a cells shape might become what is observed in figure Figure 5.6, **B**.

Chapter 6

Conclusion and Further Work

Malignant and non-malignant cells from the urinary bladder were sent though two microfluidic devices with a constriction region cross-sectional area of 10 x 10 µm^2 and 10 x 10 µm^2. Transit time, entry time and exit times were measured using a Python script. The results show that the two populations are distinguishable, in particular for microfluidic constriction channel with a 10 µm x 10 µm constrictive region. However, several challenges still remain.

Firstly, the dimensions of the channel should be reassessed, as the microfluidic device with a 7 x 7 µm^2 constriction cross-sectional area showed less difference in transit time between the two cell lines. From observation, this dimension seems to be too small to efficiently run experiments and analyze the results.

In addition to this, as suggested previously, the research would benefit from a more optimized work-flow in all aspects of the experimental work. In particular, cooling the cells after suspending them in nutrient-free PBS to improve the lifetime of the cells and extend the time prior to starvation.

In order to further improve the technique, some adjustments should be made. The analysis part of the work flow is currently the most time-consuming part, and could be more optimized. Developing a script which can distinguish concurrent cells both in parallel and in the same channel would greatly reduce the time it takes to analyze

the cells.

A digital focus set-up could also improve the ability to produce similar recordings over several experiments as the focus currently needs to be gauged by visual inspection, which can be quite unreliable.

Further, for the experimental work of this thesis, the field of view, meaning the area recorded while running experiments has been as small as possible while still observing the entire constriction in order to increase the duration of recording. While increasing duration of recording, it is impossible to assess how long cells retain their deformed shape after exiting the constriction, as the recording only observes them for a few microseconds after exiting. A larger field of view could allow the observer to see if the cells retain shape permanently or return to their initial shape after some time. This information would inform the deformation type of the cell, i.e. plastic or elastic.

Bibliography

[1] *Cancer*. URL: www.who.int/health-topics/cancer.

[2] *Kreft i Norge*. URL: kreftforeningen.no/om-kreft/kreft-i-norge/.

[3] W.M. Becker et al. *Becker's World of the Cell*. Pearson, 2006. ISBN: 0321312082.

[4] American Society of Clinical Oncology (ASCO). *Stages of Cancer*. URL: www.cancer.net/navigating-cancer-care/diagnosing-cancer/stages-cancer.

[5] P. Sundd et al. 'Pathophysiology of Sickle Cell Disease'. In: *Annual Review of Pathology: Mechanisms of Disease* 14 (2019), pp. 263–292. DOI: 10.1146/annurev-pathmechdis-012418-012838.

[6] M. Kubánková et al. 'Physical phenotype of blood cells is altered in COVID-19'. In: *Biophysical Journal* 120 (2021), pp. 2838–2847. DOI: 10.1016/j.bpj.2021.05.025.

[7] C. Faigle et al. 'A monolithic glass chip for active single-cell sorting based on mechanical phenotyping'. In: *Lab on a Chip* 15 (2015), pp. 1267–1275. DOI: 10.1039/c4lc01196a.

[8] A. Arduino et al. 'A Continuum-Tensegrity Computational Model for Chondrocyte Biomechanics in AFM Indentation and Micropipette Aspiration'. In: *Ann Biomed Eng* 50 (2019), pp. 1911–1922. DOI: 10.1007/s10439-022-03011-1.

[9] M. Lekka et al. 'Elasticity of normal and cancerous human bladder cells studied by scanning force microscopy'. In: *Eur Biophys J* 28 (1999), pp. 312–316. DOI: 10.1007/s002490050213.

[10] M. Lekka et al. 'Cancer cell recognition - Mechanical phenotype'. In: *Micron* 43 (2012), pp. 1259–1266. DOI: 10.1016/j.micron.2012.01.019.

[11] M. J. Rosenbluth et al. 'Analyzing cell mechanics in hematologic diseases with microfluidic biophysical flow cytometry'. In: *Lab Chip* 8 (7 2008), pp. 1062–1070. DOI: 10.1039/B802931H.

[12] P. M. Graybill et al. 'A constriction channel analysis of astrocytoma stiffness and disease progression'. In: *Biomicrofluidics* 15 (Mar. 2021), p. 024103. DOI: 10.1063/5.0040283.

[13] H. Lodish et al. *Molecular Cell Biology*. W.H.Freeman Co Ltd, 2016. ISBN: 9781464187445.

[14] X. Wang et al. 'Mechanical stability of the cell nucleus – roles played by the cytoskeleton in nuclear deformation and strain recovery'. In: *Journal of Cell Science* 131 (2018), jcs209627. DOI: 10.1242/jcs.209627.

[15] K. Talkenberger et al. 'Amoeboid-mesenchymal migration plasticity promotes invasion only in complex heterogeneous microenvironments'. In: *Sci Rep* 7 (2017), p. 9237.

[16] F. Sabeh et al. 'Protease-dependent versus -independent cancer cell invasion programs: three-dimensional amoeboid movement revisited'. In: *Journal of Cell Biology* 185 (Mar. 2009), pp. 11–19.

[17] V. Gensbittel et al. 'Mechanical Adaptability of Tumor Cells in Metastasis'. In: *Developmental Cell* 55 (2020), pp. 164–179. DOI: 10.1016/j.devcel.2020.10.011.

[18] D. Beebe et al. 'Physics and Applications of Microfluidics in Biology'. In: *Annual review of biomedical engineering* 4 (2002), pp. 261–86. DOI: 10.1146/annurev.bioeng.4.112601.125916.

[19] H. Bruus. *Theoretical Microfluidics*. Oxford Master Series in Physics. Oxford University Press, 2007. ISBN: 9780199235087.

[20] R.L Panton. *Incompressible Flow*. Wiley, 2013. Chap. 10, pp. 198–219. ISBN: 9781118713075. DOI: 10.1002/9781118713075.ch10.

[21] W.D. Callister and D.G. Rethwisch. *Callister's Materials Science and Engineering*. Wiley, 2020. ISBN: 9781119453918.

[22] P. Kollmannsberger and B. Fabry. 'Linear and Nonlinear Rheology of Living Cells'. In: *Annual Review of Materials Research* 41 (2011), pp. 75–97. DOI: 10.1146/annurev-matsci-062910-100351.

[23] M. Urbanska et al. 'A comparison of microfluidic methods for high-throughput cell deformability measurements'. In: *Nat Methods* 17 (2020), pp. 587–593. DOI: 10.1038/s41592-020-0818-8.

[24] S. Byun et al. 'Characterizing deformability and surface friction of canccer cells'. In: *PNAS* 110 (2013), pp. 7580–7585. DOI: 10.1073/pnas.1218806110.

[25] T. G. Hines. 'A Novel Fabrication Method for Microfluidic Constriction Devices'. Nanotechnology Specialization Project. 2022.

[26] *CleWin*. URL: wieweb.com.

[27] *ImageJ*. URL: imagej.nih.gov/ij/download.html.

[28] *Python version 3.9.13*. URL: Python.org.

[29] *OpenCV version 4.7.0*. URL: opencv.org.

[30] A. Sharfeddin et al. 'Comparison of the macroscale and microscale tests for measuring elastic properties of polydimethylsiloxane'. In: *Journal of Applied Polymer Science* 132 (2015). DOI: 10.1002/app.42680.

[31] E. Mfoumou et al. 'Tuning Polymethyldisiloxane (PDMS) properties for biomedical applications'. In: *Advanced Materials Letters* 10 (2019), pp. 107–111. DOI: 10.5185/amlett.2019.2130.

[32] S. Agaoglu et al. 'The effect of pre-polymer/cross-linker storage on the elasticity and reliability of PDMS microfluidic devices'. In: *Microfluid Nanofluid* 21 (2017), p. 117. DOI: 10.1007/s10404-017-1953-0.

[33] G. Topman et al. 'A method for quick, low-cost automated confluency measurements'. In: *Microsc Microanal* 17 (2011), pp. 915–922. DOI: 10.1017/S1431927611012153.

[34] S.E. Cross et al. 'AFM-based analysis of human metastatic cancer cells'. In: *Nanotechnology* 19 (2008), p. 384003. DOI: 10.1088/0957-4484/19/38/384003.

Appendix

Appendix A - Python Code

```
import cv2 as cv
import numpy as np
import math
import pandas as pd
from pathlib import Path
import os



videonavn = '50'
a_path = path_to_video_folder
b_file = videonavn
c_extension = '.csv'
joined_path = os.path.join(a_path, b_file + c_extension  )

filepath = Path(joined_path)
filepath.parent.mkdir(parents=True, exist_ok=True)



vid = cv.VideoCapture('Videos/HCV29/10/'+ videonavn + '.avi') #Path
 ↪  to video
number_of_frames = vid.get(cv.CAP_PROP_FRAME_COUNT) #Find the
 ↪  number of frames in the video
#result_vid = cv.VideoWriter(videonavn + '.avi',
 ↪  cv.VideoWriter_fourcc(*'MJPG'), 10.0, (int(vid.get(3)),
 ↪  int(vid.get(4)))) #Writes a video, to save a copy of the
 ↪  contoured video.
```

```
ret, frame1 = vid.read()
ret, frame2 = vid.read()
df = pd.DataFrame(columns=['frame number', 'initial area','cv_area'
↪  , 'entry time', 'constricted time', 'exit time', 'minor axis',
↪  'major axis', 'constricted', 'pos', 'ypos', 'velo' ])

#Declaration of variables
k = []
j = []
l = []
i = 0
lol = {}
tid = 0
teller_entry = 0
framelist = []
mal = []
teller_outry = 0
major_axis_list = []
area_init = []
area_fin = []
constricted = []
pos = []
enter_exit_frames = []
p = 0
entering_frames = []
constricted_frames = []
exiting_frames = []
y_pos_diff = []


#Function to get and draw contours
```

```
def getContours(img, imgContour):
    contours, hierarchy = cv.findContours(img, cv.RETR_EXTERNAL,
    ↪  cv.CHAIN_APPROX_NONE)
    y_pos_line1 = cv.getTrackbarPos("Upper Position", "Parameters")
    ↪  #BLUE
    y_pos_line2 = cv.getTrackbarPos("Lower Position", "Parameters")
    ↪  #RED
    cv.line(imgContour, (0,y_pos_line1), (1000,y_pos_line1), (255,
    ↪  0, 0), 1)  #BLUE
    cv.line(imgContour, (0,y_pos_line1+int(300* (1/0.87619))),
    ↪  (1000,y_pos_line1+int(295*(1/0.87619))), (0, 0, 255), 1)
    ↪  #RED
    cv.putText(imgContour, " %.0f" % (i) + "/%.0f" %
    ↪  (number_of_frames-1), (0, 35), cv.FONT_HERSHEY_COMPLEX, 0.5,
    ↪  (50, 175, 0), 2 ) #Puts text in the frame.


    for  cnt in contours:  #Iterate through all found contours
        global df
        area = cv.contourArea(cnt) #Calculates the pixel area of
        ↪  the found contour.
        if area  > 100: #Only draw contours if certain area is
        ↪  larger than
            cv.drawContours(imgContour, contours, -1, (0, 255, 0),
            ↪  1) #Draws contours on imgContour.
            peri = cv.arcLength(cnt, True)
            approx = cv.approxPolyDP(cnt, 0.02 * peri, True)
            x, y, w, h = cv.boundingRect(approx) #Used to place
            ↪  text
            elipse = cv.fitEllipse(cnt) #Approximates the contour
            ↪  as a ellipse
```

```
(xc, yc), (d1, d2), angle = elipse #Extracts values
↪  from ellipse. d1, d2 are minor and major
↪  diameters.

#Draw elipse in green
cv.ellipse(imgContour, elipse, (0,255,0), 1)
xc, yc = elipse[0] #Find centerpoints

#Draw major axis in red
rmajor = max(d1,d2)/2 #Find which is major and minor
↪  axis. Divides it by two, giving the radius.
if angle > 90:
    angle = angle - 90
else:
    angle = angle + 90

x1_major = xc + math.cos(math.radians(angle))*rmajor
y1_major = yc + math.sin(math.radians(angle))*rmajor
x2_major = xc + math.cos(math.radians(angle+180))*rmajor
y2_major = yc + math.sin(math.radians(angle+180))*rmajor
cv.line(imgContour, (int(x1_major), int(y1_major)),
↪  (int(x2_major), int(y2_major)), (0, 0, 255), 1)
↪  #Draws a red line for the major axis.

majorAxis_length = rmajor*0.87619 #Radius in um.
↪  0.87619 found to be the scaling factor for my
↪  images (20X mag)

#Draw minor axis in blue
rminor = min(d1, d2)/2
if angle > 90:
```

```
        angle = angle - 90
else:
    angle = angle + 90

x1_minor = xc + math.cos(math.radians(angle))*rminor
y1_minor = yc + math.sin(math.radians(angle))*rminor
x2_minor = xc + math.cos(math.radians(angle+180))*rminor
y2_minor = yc + math.sin(math.radians(angle+180))*rminor

cv.line(imgContour, (int(x1_minor),int(y1_minor)),
↪  (int(x2_minor),int(y2_minor)), (255, 0, 0), 1)
minorAxis_length = rminor*0.87619

#Displaying text for minor and major axis along each
↪  contour (cell).
cv.putText(imgContour, "R_major: %.2f" %
↪  round(majorAxis_length, 2)  + " um", (x+w + 20, y
↪  +45), cv.FONT_HERSHEY_COMPLEX, 0.7, (0, 205, 0), 2 )
cv.putText(imgContour, "R_minor:  %.2f" %
↪  round(minorAxis_length, 2)+ " um", (x+w + 20, y
↪  +65), cv.FONT_HERSHEY_COMPLEX, 0.7, (0, 205, 0), 2)



if((y+h >= y_pos_line1) and ((y) <= y_pos_line1)):
    constriction_occupied = False
    cv.putText(imgContour, "Status: Entering", (x+w +
    ↪  20, y +105), cv.FONT_HERSHEY_COMPLEX, 0.7, (0,
    ↪  205, 0), 2)
    k.append(i)
    y_print = yc - y_pos_line1
```

```
lol[i] = []
lol[i].append(y_print)

val = lol.get(i-1, [0])
val2 = lol.get(i, [0])
diff = 0
if val[0] != val2[0] and val2[0] > val[0] and val[0]
↪  != 0 and val2[0] != 0:
    diff = val2[0] - val[0]
velo =  (diff/0.001) * 0.87619
y_posisjon = y_print*0.87619
new_row1 = pd.DataFrame({
'frame number' : [i],
'initial area' : ['-'],
'cv_area' : ['-'],
'entry time' : [1/1000],
'constricted time': [' '],
'exit time' : ['-'],
'minor axis' : [minorAxis_length],
'major axis' : [majorAxis_length],
'constricted' : [False],
'pos' : ['Entering'],
'ypos' : [y_posisjon],
'velo' : [velo]


},  dtype='object')
new_row1['constricted'] =
↪  new_row1['constricted'].astype(bool)
df = pd.concat([df, new_row1], ignore_index=True)
```

```
prev_center = xc, yc

if(y > y_pos_line1 and y+h < y_pos_line2):
    constriction_occupied = True
    cv.putText(imgContour, "Status: Constricted", (x+w +
    ↪  20, y +105), cv.FONT_HERSHEY_COMPLEX, 0.7, (0,
    ↪  205, 0), 2)
    j.append(float(i))
    y_print = yc - y_pos_line1
    lol[i] = []
    lol[i].append(y_print)

    val = lol.get(i-1, [0])
    val2 = lol.get(i, [0])

    diff = 0
    if val[0] != val2[0] and val2[0] > val[0] and val[0]
    ↪  != 0 and val2[0] != 0:
        diff = val2[0] - val[0]
    velo =  (diff/0.001) * 0.87619
    y_posisjon = y_print*0.87619

    new_row2 = pd.DataFrame({
    'frame number' : [i],
    'initial area' : ['-'],
    'cv_area' : ['-'],
    'entry time' : [' '],
    'constricted time': [1/1000],
    'exit time' : ['-'],
    'minor axis' : [minorAxis_length],
    'major axis' : [majorAxis_length],
```

```
            'constricted' : [True],
            'pos' : ['Constricted'],
            'ypos' : [y_posisjon],
            'velo' : [velo]


        }, dtype='object')
        new_row2['constricted'] =
        ↪  new_row2['constricted'].astype(bool)
        df = pd.concat([df, new_row2], ignore_index=True)


    if((y+h >= y_pos_line2) and (y <= y_pos_line2)):
        constriction_occupied = False
        exiting = True
        cv.putText(imgContour, "Status: Exiting", (x+w + 20,
        ↪  y +105), cv.FONT_HERSHEY_COMPLEX, 0.7, (0, 205,
        ↪  0), 2)
        l.append(i)
        y_print = yc - y_pos_line1
        lol[i] = []
        lol[i].append(y_print)


        val = lol.get(i-1, [0])
        val2 = lol.get(i, [0])

        diff = 0
        if val[0] != val2[0] and val2[0] > val[0] and val[0]
        ↪  != 0 and val2[0] != 0:
            diff = val2[0] - val[0]
```

```
            velo =  (diff/0.001) * 0.87619
            y_posisjon = y_print*0.87619


            new_row3 = pd.DataFrame({
            'frame number' : [i],
            'initial area' : ['-'],
            'cv_area' : ['-'],
            'entry time' : [' '],
            'constricted time': [' '],
            'exit time' : [1/1000],
            'minor axis' : [minorAxis_length],
            'major axis' : [majorAxis_length],
            'constricted' : [False],
            'pos' : ['Exiting'],
            'ypos' : [y_posisjon],
            'velo' : [velo]

            },  dtype='object')
            new_row3['constricted'] =
            ↪  new_row3['constricted'].astype(bool)
            df = pd.concat([df, new_row3], ignore_index=True)


        if y+h < y_pos_line1:
            ellipse_areal =
            ↪  minorAxis_length*majorAxis_length*np.pi
            new_row4 = pd.DataFrame({
            'frame number' : [i],
            'initial area' : [ellipse_areal],
            'cv_area' : [area*(0.87619**2)],
```

```
                'entry time' : [' '],
                'constricted time': ['-'],
                'exit time' : ['-'],
                'minor axis' : [minorAxis_length],
                'major axis' : [majorAxis_length],
                'constricted' : [False],
                'pos' : ['N'],
                'ypos' : ['-'],
                'velo' : ['-']

                }, dtype='object')
                new_row4['constricted'] =
                ↪  new_row4['constricted'].astype(bool)
                df = pd.concat([df, new_row4], ignore_index=True)
def empty(a):
    pass

cv.namedWindow("Parameters")
cv.resizeWindow("Parameters", 640,240)
cv.createTrackbar("Threshold 1", "Parameters", 39,255, empty)
cv.createTrackbar("Threshold 2", "Parameters", 72,255, empty)
cv.createTrackbar("Upper Position", "Parameters",72, 1000, empty)
cv.createTrackbar("Lower Position", "Parameters", 440, 1000, empty)


while vid.isOpened(): #Iterating through the frames
    i += 1 #Counting the frames

    #Image Processing
    imgContour = frame1.copy()
```

```
gray_frame1 = cv.cvtColor(frame1, cv.COLOR_BGR2GRAY) #Converts
↪  to grayscale
gray_frame2 = cv.cvtColor(frame2, cv.COLOR_BGR2GRAY)

diff = cv.absdiff(gray_frame1, gray_frame2)
lower_threshold = cv.getTrackbarPos("Threshold 1", "Parameters")
upper_threshold = cv.getTrackbarPos("Threshold 2", "Parameters")

ret2, th2 = cv.threshold(diff,10,125, cv.THRESH_BINARY) #20,125

ret3, th3 = cv.threshold(th2, 0,250,
↪  cv.THRESH_BINARY+cv.THRESH_OTSU)

kernel_dil = np.ones((3,3))
kernel_erode = np.ones((2,2))

dilated = cv.dilate(th3, kernel_dil, iterations=1)
eroded = cv.erode(dilated, kernel_erode, iterations=2)

getContours(eroded, imgContour)

cv.imshow("vid", imgContour)

#result_vid.write(imgContour)
frame1 = frame2
ret, frame1 = vid.read()

if cv.waitKey(20) & 0xFF==ord('d'):
    break
if i == int(number_of_frames)- 1:
    break
```

```
print("Analysis completed")
vid.release()
#result_vid.release()
df.to_csv(filepath, index = False)
cv.destroyAllWindows()
```

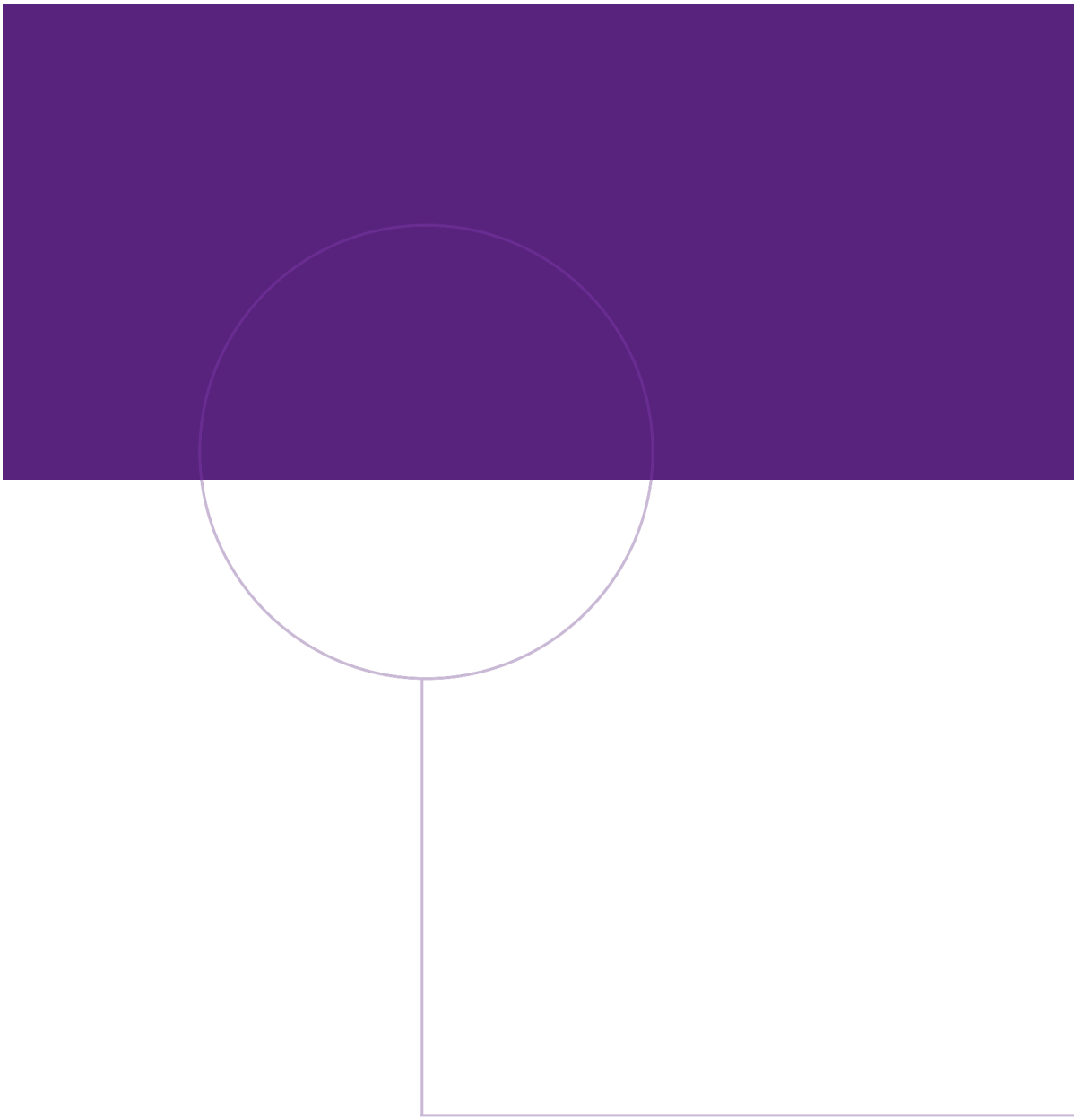

NTNU

Norwegian University of
Science and Technology